MECHANICAL PROPERTY EVALUATION OF MAGNESIUM RICH PRIMER COATING SYSTEM OVER AA2024 T-3 ALUMINUM ALLOY BY NANO-INDENTATION

by

HONGYI QU

THESIS

Submitted in partial fulfillment of the requirements
For the degree of Master of Science in Mechanical Engineering at
The University of Texas at Arlington
August, 2016

Arlington, Texas

Supervising Committee:

Bo Yang, Supervising Professor
Wen Chan
Seiichi Nomura

ACKNOWLEDGEMENTS

Foremost, I would like to express my sincere gratitude to my supervising professor Dr. Bo Yang for the continuous support of my research and experiment. His guidance helped me in all the time of research, experiment and writing of the thesis.

Besides my advisor, I would like to thanks the rest of my thesis committee: Dr. Wen Chan and Dr. Seiichi Nomura for their encouragement, insightful comments.

My sincere thanks also goes to Dr. Jianchao Jiang and Prof. Meng for offering me the experiment facility in UTA CCMB lab.

LIST OF FIGURES

LIST OF TABLES

ABSTRACT

MECHANICAL PROPERTY EVALUATION OF MAGNESIUM RICH PRIMER COATING SYSTEM OVER AA2024 T-3 ALUMINUM ALLOY BY NANO-INDENTATION

Hongyi Qu, Master of Science

The University of Texas at Arlington, 2016

Supervising Professor: Bo Yang

Aluminum alloy is widely used as a major structural material, such as for wing and fuselage, in aerospace industry. Corrosion is the most insidious form of damage to aluminum alloy, which can cause aircraft structure damage and related safety issue. Coating is generally used in industry to protect metal structure. An alternative to present toxic chromium primer coating system, magnesium rich primer (MgRP) has been developed to protect AA 2024 T-3. Studies have demonstrated the anti-corrosion performance of MgRP. However, the interlayer material heterogeneity can affect the mechanical properties of coating such as modulus, hardness and interfacial behavior.

In the present study, AA 2024-T3 samples with both chromium primer and magnesium primer coating systems are examined experimentally and computationally. The nanoindentation experiment in combination with finite element analysis (FEA) shows that the mechanical properties of the top coating are not affected by interlayer material heterogeneity under low

indentation loading, 10,000 μN. However, if the indentation force is increased to 60,000 μN, delamination could occur at the MgRP. FEA results show the apparent differences in the maximum principal stress value and location in MgRP compared with chromium coating. It is explained by the fact that the larger magnesium particles in MgRP lead to greater stress concentration at the particle boundary. The greater stress induces delamination.

Table of Contents

Chapter 1 Introduction

Various types of metals are used in different fields, such as aerospace industry, mechanical industry, petroleum industry, electric industry and even used in the human body as support or replacements. Only copper and the precious metals of 85 metals in the Periodic Table can be found in nature in their metallic state [1]. All others, whatever the usage is, tend to react with their environment to different extents and rates. The metal will release the electron to be free metal ions and react to become its compound forms. The process for the chemical reaction called corrosion, which is a naturally occurring phenomenon and destruct metal from a chemical or electrochemical reaction with its environment.

Aluminum alloy is wildly used in aerospace industry as major structural material since the 1900's [15]. However, aluminum alloy has localized corrosion problems which can accelerate structural failure and cause serious accident. On December 15, 1967, silver bridge in Ohio suddenly collapsed into the Ohio River. Stress corrosion cracking combined with corrosion fatigue occurred and the aluminum structure failed after suffering the stress cycle [2]. On April 28, 1988, Aloha Airlines Flight 243 suffered explosive decompression at 24,000 feet caused by metal fatigue which was exacerbated by corrosion [3]. In 1995, ASA flight 529 lost a propeller and crash-landed in Georgia. In 2013, Manchester Airport crew perform an emergency stop during takeoff due to engine flashing and power loss due to a High cycle fatigue crack propagated from a corrosion initiation site [4]. These are but a few examples as to how corrosion impact human life particularly in aircraft industrial.

Since corrosion causes deterioration of most concrete metal applications, multiple protection strategies have been developed to reduce and retard the corrosion including catholic protection

and corrosion inhibitors. A coating covered that applied metal surface are increasingly being applied in last two decades [5]. The resulting coating is often characterized with respect to permeability and morphological and mechanical properties [6].

In current aircraft industry, a chromate rich multi-layer coating are widely used to protect aluminum alloy as a primer layer covered over pretreated surface aluminum alloy and it is being replaced by an alternative coating material magnesium rich primer since the carcinogen, toxic and mutagenic of Cr (VI) ion. Although, anti-corrosion ability of magnesium rich primer has been approved [16], the mechanical properties of magnesium rich primer coating system including elastic, elastic-plastic and interface failure is not determined,

In this thesis, nano-indentation experiment was applied to determining the mechanical property for the AA2024 T-3 with different coating layer. Meanwhile, finite element analysis has been employed to model the nano-indentation experimental process and developed to predict the interface behavior of the coating system. Both experimental and numerical method are adopted to provide a systematic method for mechanical properties on coating system.

1.1 Fundamentals of Corrosion

Corrosion is the result of an electrochemical phenomenon including both anodic reaction and a cathodic reaction. The metal ion goes in to the solution from anode and reacted at cathode to release the electrons. Two complementary reactions are occurred inside the electrolyte of an electrolytic cell.

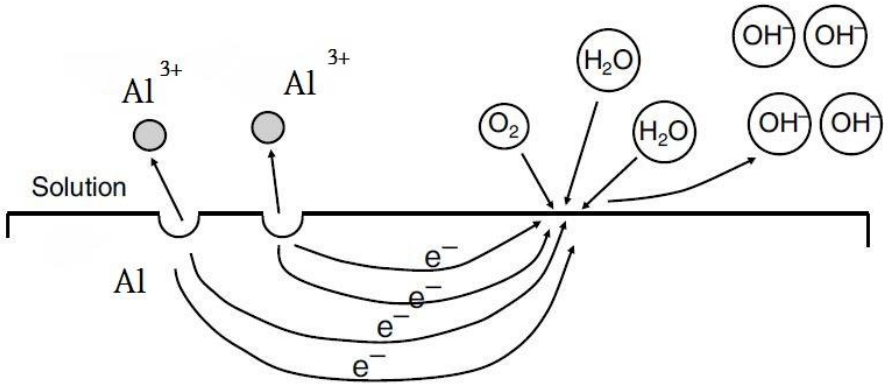

Figure 1 Basic Principle of Aluminum Corrosion Process [6]

There are various type of corrosion that deteriorate metals including uniform attack, galvanic attack, crevice corrosion, pitting, inter-granular corrosion, selective leaching, erosion corrosion and stress corrosion [6]. Metal Corrosion is generally occurred on the corroded metal surface, anodic and cathodic reactions occur in a coupled manner at different place on the metal surface. In acidic aqueous environment, metal reacts with $H^+(aq)$ to yield atomic hydrogen. In alkali aqueous environment, the iron reacts with $OH^-(aq)$ to form ferrous hydroxide.

Table 1 Examples of Anodic and Cathode Corrosion Reactions

Anodic Reaction	**Cathodic Reactions**
$Fe(s) \rightarrow Fe^{2+}(aq) + 2e^-$	
$Al(s) \rightarrow Al^{3+}(aq) + 3e^-$	$2H^+(aq) + 2e^- \rightarrow H_2(g)$
$2Cu(s) + H_2O \rightarrow Cu_2O(s) + 2H^+(aq) + 2e^-$	$O_2(g) + 2H_2O + 4e^- \rightarrow 4OH^-(aq)$

1.2 Corrosion Control

Corrosion protection system is to prevent and retard the corrosion process such as provide useful service life of protective elements or components. Several different corrosion protection methods have been developed which can be defined as two basic types. They are changing the electrode potential of the metal surface and changing the nature of the metal itself. Anodic protection and cathodic protection are generally using for corrosion control by changing the electrode potential.

1.2.1 Cathodic protection

The principle for cathodic protection is to change the electrode potential of the metallic article or structure, which was first described by T. Roy [8]. The nature of the metal can be changed through the use of metallic coating or by material selection in which a corrosion-resistant alloy is chosen over a less corrosion-resistant one [12]. Thomas Edison experimented with impressed current cathodic protection on ships in 1890 but was unsuccessful due to lack of a suitable current source and anode material. In U.S., cathodic protection was applied to oil natural gas industry by 1945 [9]. It prevents the oxidation process from occurring by creating a current flow from the cathodic protection system to the structure. Two basic types system, sacrificial anode and impressed current, are applied for current CP application.

1.2.1.1 Sacrificial anode system

The sacrificial anode is made from a metal with more negative electrochemical potential than the protected metal. The potential difference drive the sacrificial anode material corrodes in the system.

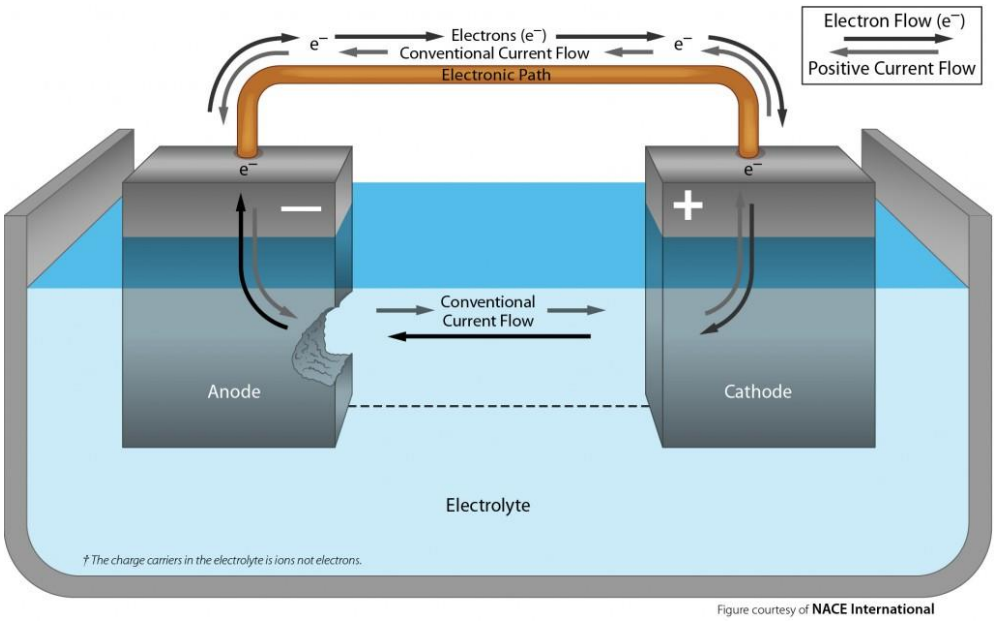

Figure 2 Principle of Sacrificial Anode System [23]

As shown in figure 2, sacrificial anode system must have two conditions existing besides the anode and the cathode. A return current path for the electrons is needed to flow from the anode to the cathode. Physical contact or an electrolyte is accepted to convey the electrons.

Easy to install, low voltage and current and no external power source are apparent for sacrificial anode systems. However, limited current capacity based on the mass of anode restrict the performance of the system applied in high-resistivity environment including increased weight of protected units or increased air or water flow on the units.

Table 2 Galvanic Series

Galvanic Series (Top Most Reactive/Anodic)
Magnesium
Zinc
Aluminum
Iron, Plain carbon and low alloy steels
Lead, high lead alloys
Tin Plate
Chromium plated materials, Chromium alloys
Brass
Copper
Nickel
Stainless steels
Silver
Gold

The galvanic corrosion protection depends on the electrical potential between the two metals. The Galvanic Series orders metals based on the potential they exhibit in seawater. The most reactive are at the top of the table and the lease reactive at the bottom

1.2.1.2 Impressed current systems

Larger structures, which are not capable of delivering ample current to anode offering protection, are made cathodic by electrically connection to anode in the same electrolyte through a source of direct electric current for a long term service.

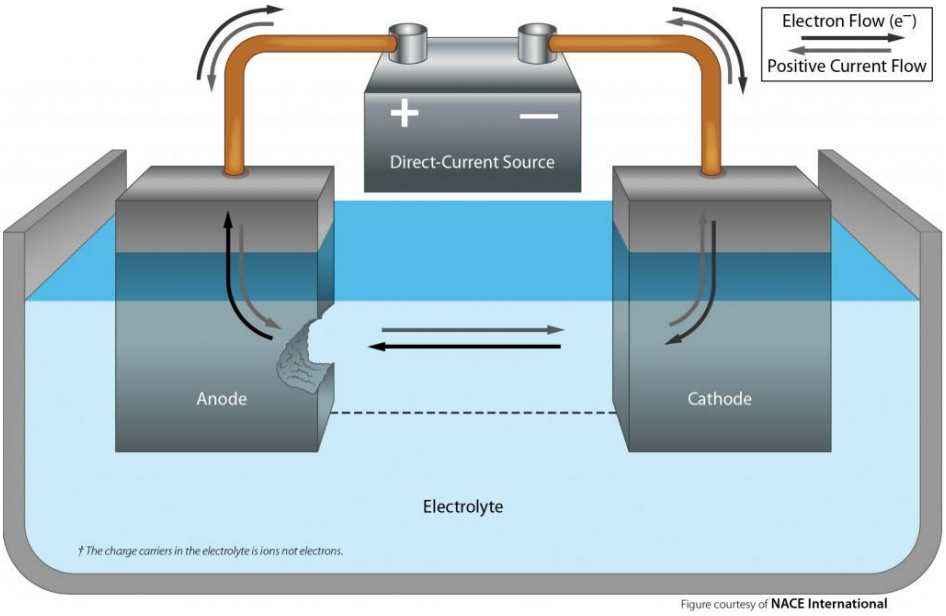

Figure 3 Principle of Impressed Current Systems [23]

As shown in figure 3, an impressed current is applied in opposite direction to nullify the corrosion current and convert the corroding metal from anode to cathode. The output DC positive cable is connected to the anodes, and negative cable is connected to the protected structure. The ICCP system should be optimized to provide enough current in order to perform sufficient protection. However, in order to retaining some other desirable property, cathodic protection is not an option to maintain the requirement material property. In such cases, using corrosion inhibitors to alter the environment becomes a method of corrosion control

1.2.2 Corrosion inhibitors

In General, foreign molecules are strongly effect the surface reaction in surface chemistry, which can be controlled by compounds known as inhibitors which adsorb on the reacting metal surface [10]. Inhibitors are substances or mixtures, which are added in a small concentration to aggressive environmental inhibits, prevent or minimize the corrosion [11]. Growing usages of corrosion inhibitors in various industrial was noted by Hackeman [14] in Table 3.

Table 3 Industrial Applications of Corrosion inhibitors [14]

Application	inhibitors
Potable water	$CaCO_3$ deposition, Silicates, Polyphosphates
Recirculating cooling water	Chromates, Nitrates, Polyphosphates, Silicates, Zinc salts, Benzotriazole
Automotive engine coolant system	Borax-nitrite mixtures, Sodium mercaptobenzothiazole, Benzotriazole
High-chloride solutions	Chromates, sodium nitrite, chromate-phosphate mixtures
Acid pickling	Various amines, Pyridine, Quinolone, Mercaptans, Phenylthiourea
Oil recovery	Primary, Secondary, Tertiary Amines, Diamines, Amides, Polyethoxylated Amines
Steel-reinforced concrete	Calcium Nitrite, Sodium Benzoate
Surface treatment of metals	Chromates
Auto body steel sheet	Phosphates

Inhibitors can be defined as passivation inhibitors, organic inhibitors, precipitation inhibitors and vapor phase inhibitors. They are all usually able to prevent general or uniform corrosion. Corrosion can be predicted and life spans of corrosion rates reduced by the use of inhibitors.

$$I_{eff} = \frac{R_o - R_1}{R_o} \tag{1.1}$$

Where, I_{eff} is the efficiency of the inhibitor, R_o is the corrosion rate of the metal without inhibitor present and R_1 is the corrosion rate of the metal with inhibitor present. Both R_o and R_1 could be defended by corrosion testing techniques

1.3 Aluminum Alloy in Aerospace Industry

Aluminum alloy is wildly used in aerospace industry as major structural material since the 1900's [15]. Aluminum alloy has an excellent electric conductivity, high strength and relatively low weight, the specific weight is 2.7 g/cm^3, which is only one-third of steel. It also exhibits excellent corrosion resistance property after their surface reacting with air to form a passive layer (Al_2O_3). Further, the low manufacturing cost makes it being the most suitable for aircraft material.

Aluminum alloys such as 7000 and 2000 series have the ability to resist high temperature and high pressure, which has advanced and stable use in aerospace application. For instance, AA 7075-T6 is used in aircraft wing structure and AA 2024-T3 is used in the fuselage [16, 17].

Table 4 AA2024 T-3 Element Compositions [18]

Element	**Composition**
Copper	3.8-3.9
Magnesium	1.2-1.8
manganese	0.3-0.9
silicon	0.5
chromium	0.1
Zinc	0.25
Titanium	0.15
Aluminum	93.2-90.9

As shown in table 4 that AA 2024 T-3 contains as much as 3.5 % copper and 1.5 % magnesium in aluminum, which can be dissolved during heat treatment, as a result of high solubility. AA 2024 T-3 also has much higher tensile strength than that of pure aluminum.

Table 5 Mechanical Properties of Steel, Aluminum and Aluminum Alloy

Materials	**Steel**	**Aluminum**	**Aluminum Alloy**	
Series No.	AISI 4340	110	2024 T-3	7075 T-6
Density (g/cm^3)	7.8	2.7	2.8	2.8
Tensile Strength (MPa)	1790	90	485	550
Yield Strength (MPa)	1483	34	345	485
Elasticity Modulus (GPa)	200	68	72	71

However, the relatively high copper content leaves the alloy highly susceptible to localized corrosion. The dark area of the SEM image shown in figure 4 a) shows copper rich regions and the bright areas represent the aluminum rich regions, where micro structure give rise to galvanic couple [20], pitting corrosion on the surface of AA 2024-T3 showing in figure 4 b) initiates surrounding the alloy matrix. The copper region present in the grain boundaries as $CuAl_2$ during solidification process.

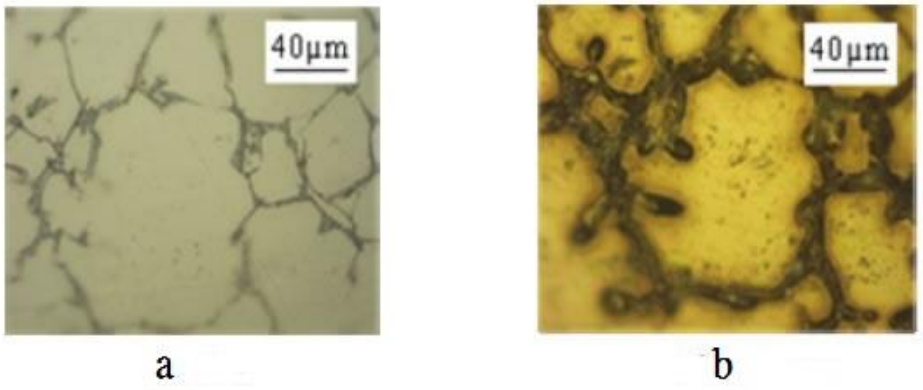

Figure 4 SEM Images of AA 2024 T-3 a) Before Corrosion b) After Corrosion [19]

It can be observed from table 2 that copper is more noble metal than aluminum, the copper rich reign surrounding the aluminum matrix react as cathode. Thus, aluminum oxidation products occurred along the aluminum matrix boundary.

The most common methods to protect aerospace aluminum alloy is applying an organic coating layers on the substrate [21]. The applied coating can protect the substrate away from physicochemical, electrochemical and adhesion mechanism [22].

Generally, there are three layers consisted in coating system, substrate surface pretreatment, conversion coating/primer and a urethane topcoat.

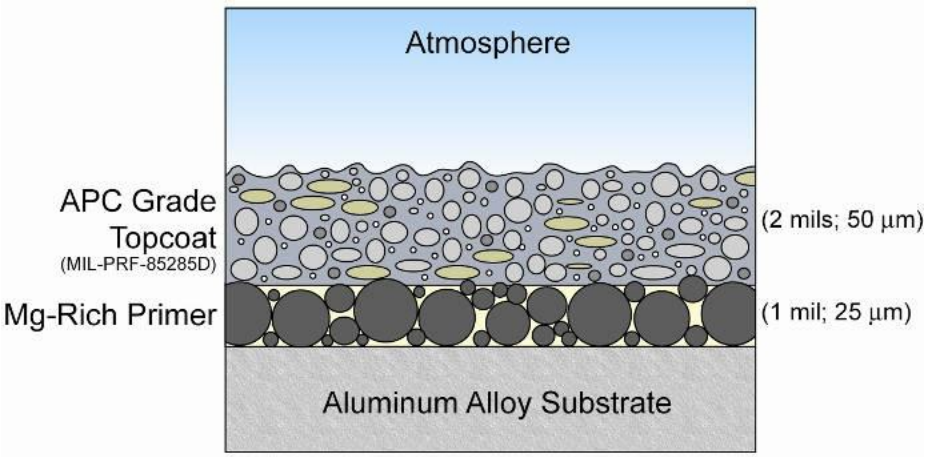

Figure 5 Schematic Cross-section of Magnesium Rich Primer Based Coating System for Corrosion Protection of Aluminum Alloys [23]

As shown in figure 5, APC grade topcoat (MIL-PRF-85285D) , where polyurethane is commonly adopted, works as the main barrier to protect the aluminum alloy from the corrosive factor such as oxygen, moisture and ultra-violet rays. The thickness for top coating varies from 50 to 200 µm. the primer layer, which improves the adhesion between coating and substrate, usually contain a pigmented organic resin matrix, the thickness for aircraft usage of the layer is about 25 µm [23].

Chromate conversion coating (CCC) or chromate pigment organic coating widely used as the most reliable method primer to protect AA2024 T-3 alloy[24,25]. Cr (III) ions, which form respective hydrophobic hydroxides, is generated due to the aluminum reacted with fluoride ions and Cr (IV) on the aluminum surface [26]. Further electrochemical reactions are blocked due to Cr (VI) ions which are contained in the hydrophobic hydroxides layer form oxides along the corrosion site [27].

Although chromium primer is chemically resistant to most compounds and offers excellent corrosion protection, it is being replaced by other pigments since it is a carcinogen, toxic and mutagenic ion. Among all those new coating products, Magnesium rich primer was established by Bierwagen [28] according to the line of zinc rich primer protection steel system [31].

Magnesium rich primer (MgRP) has shown good performance in the field which designed to couple the Mg pigment in the primer to the AA2024-T35 to provide sacrificial anode to protect aluminum alloy and offer barrier protection to the substrate [29].

Table 6 Mechanism of Aluminum Cathodic Corrosion [30]

Aluminum cathodic corrosion	Mechanism cathodic corrosion
$2Al + 3H_2O \rightarrow Al_2O_3 + 3H_2$ $Al_2O_3 + 2OH^- \rightarrow 2AlO_2^- + 3H_2O$ $O_2 + 2H_2O + 4e^- \rightarrow 4OH^-$	$Mg + 2H_2O \rightarrow Mg^{2+} + 2OH^- + H_2$

Mechanism is more reactive then aluminum, the reaction with water will increase the PH range in which aluminum is soluble [30].

1.4 Nano-indentation technology

Nano-indentation is a technique to measure mechanical properties of materials at a very small, such as thin films and continuous record of the applied load and displacement is made during indentation. It has been widely used to investigate the mechanical property of coated systems [31] and can obtain a range of mechanical properties including young's module, hardness and fracture toughness.

Compared to traditional indentation methods, nano-indentation can not only reduces the test scale but also estimate mechanical damage process such as pile-up, cracking, delamination, phase transformation etc.

Chapter 2 Experiment Instrumentations and Theories

2.1 Experiment Instrumentations

2.1.1 Nano-indentation Equipment

The nano-indentation equipment used in this experimental is a Hysitron Ubi® system manufactured by Hysitron Incorporated. The system is consisted by three major hardware components including physical indentation system in acoustic enclosure, electronics rack and computer data acquisition system.

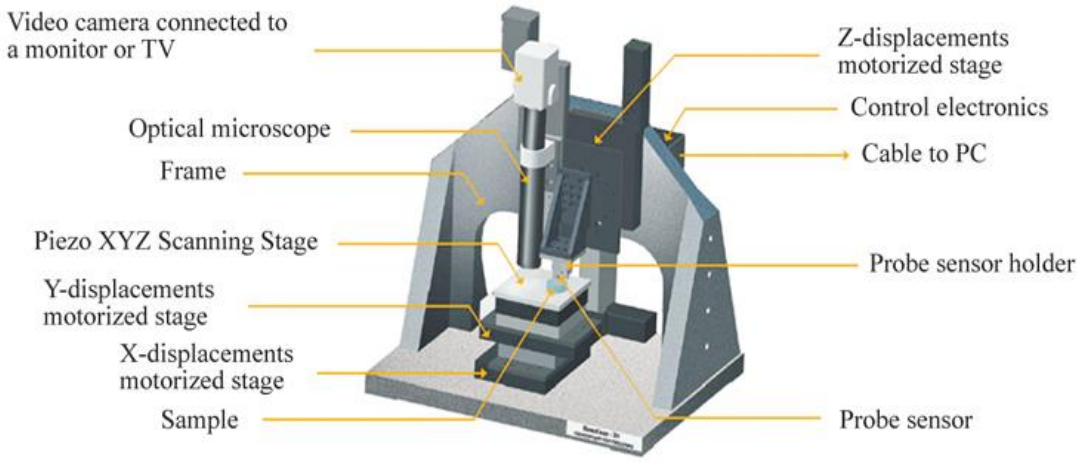

Figure 6 Nano-indenter Components [33]

Granite base in indentation system is connected with xyz staging system, optical camera system and piezo scanner. XY stage can control the sample's horizontal and vertical move, Z stage controls tip moving upward and downward to adjust the position for selection indentation area associated with living optical camera, which is mounted to the Z stage and moving with tip together, to determine the tip initial position optically.

Electronics rack system including stage controller, transducer controller and piezo controller. They can convert electric signal from PC to XYZ staging move and detect Z-axis electrostatic force to feedback to PC.

Computer data acquisition system is a user friendly system which can set up testing condition, recording and analysis the feedback testing data.

2.1.2 Types of indenter

There are serval types indenters used in Nano-indentation tests including spherical, conical, Vickers, and Berkovich indenters as shown in figure 7

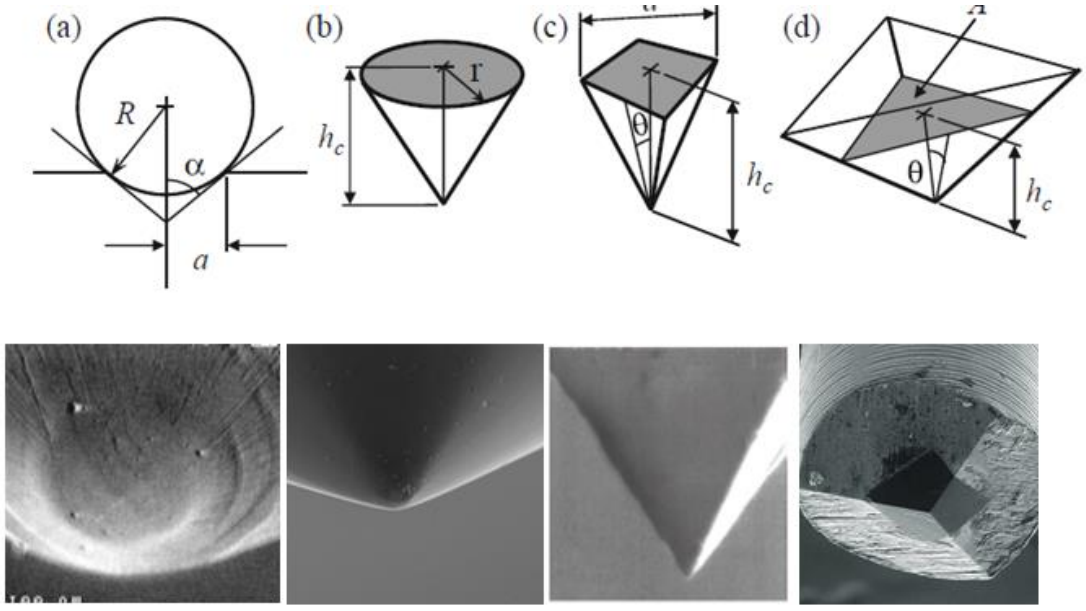

Figure 7 Indentation parameters and SEM
(a) spherical, (b) conical, (c) Vickers, and (d) Berkovich indenters

Berkovich indenter with 64.27 face angles is selected in this experiment which gives the same projected area-to-depth ration as the Vickers indenter.

2.1.3 Scanning Electron Microscope and Optical Microscope

Since the nano-indentation is nm scale experiment, optical microscope, which only have the best of 0.2 microns resolution cannot be applied to observe the nano-indentation.

Hitachi S-3000N Variable Pressure SEM, which has 3.0 nm resolutions at high vacuum, was used in the experiment to observe coating layer and surface molecular distribution.

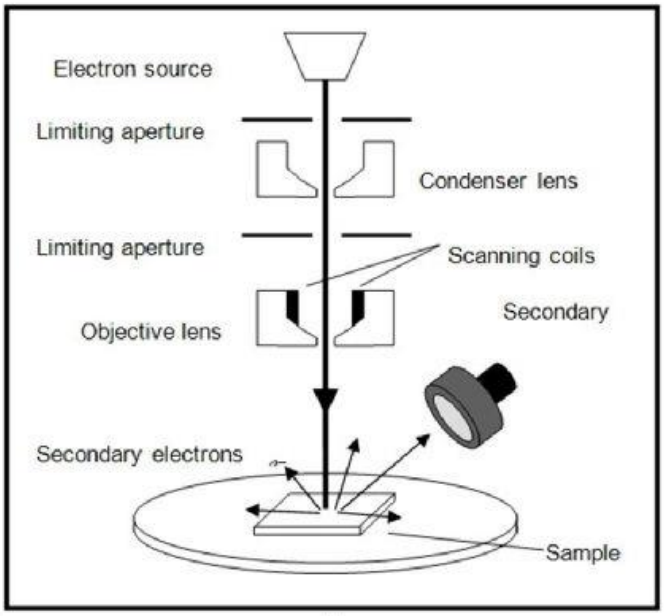

Figure 8 Schematic Diagram of an SEM [32]

The different atoms located at various depths in the sample surface has different electrical property which can generate different signal (secondary electrons) after interacting with an focused electron beam. Alternatively, there are some of the electrons in the electron beam has scattered y atoms, these high energy electrons called back scattered electrons (BSE) are rebound from the sample surface. BSE is increased by the size of the atom nucleus increased, large size atom uncles can increase BSE number which can be reflected on the image by brightness, and

higher BSE number has the brighter signal. Thus the surface property and image can be reflected by scanning the beam positon associated with detecting BSE.

2.1.4 Optical microscope

Nikon Eclipse ME600 Optical microscope is applied to observe top coating surface behavior which is made by polyurethane organic polymer has low electrical conductivity.

2.2 Experiment Theories

2.2.1 Hertz Contact Mechanic

Hertz established the original contact theories to define the elastic deformation between two solid spheres during their axial contact [34]. The radius of circle contact area (a in figure 9) can be calculated by known applied force ($F_{applied}$ in figure 9) and radius for both of contact spheres.

(a) Original representation of Hertz contact problem

(b) Elastic deformation when a force is applied over to the sphere

Figure 9 Original Hertz contact model [35]

$$a^3 = \frac{3F_{applied}R}{4E^*} \tag{2.1}$$

Where, R is their relative radius given by:

$$\frac{1}{R} = \frac{1}{R_1} + \frac{1}{R_2} \tag{2.2}$$

E^* is referred as reduced modulus given by:

$$\frac{1}{E^*} = \frac{(1-v^2)}{E} + \frac{(1-v'^2)}{E'} \tag{2.3}$$

Based on the original hertz model, the bottom sphere can be extended to a flat surface for nano-indentation mode which is most fundamental and wildly used model in nano-indentation experiments.

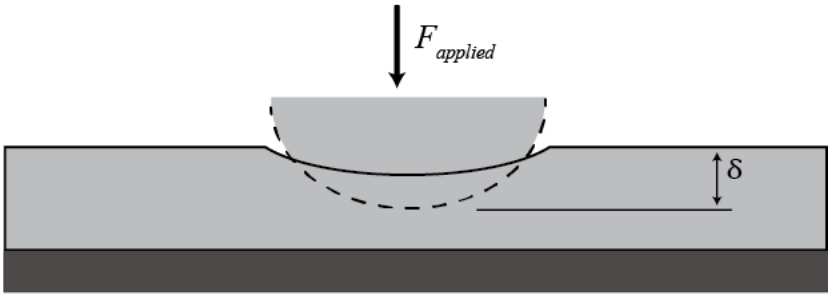

Figure 10 Equivalent Geometry of Hertz Contact Model for Nano-indentation [35]

When the indenter geometry and material is known, using recorded load-displacement data the spaceman material property E can be defined with an assumed Poisson's ratio v, the Poisson ratio can be assumed as 0.25 according to Mesarovic and Fleck [36] defined that Poisson's ratio has a minor effect on the indentation results.

However, not only elastic deformation but also elastic-plastic and plastic are occurred during indentation procedure. As shown in figure 10 hydrostatic plastic zone is generated by the indenter contact. The stress distribution cannot drive the whole material plastic but the penetration addressed pressure radiation to the region surrounding the plastic and cause elastic deformation.

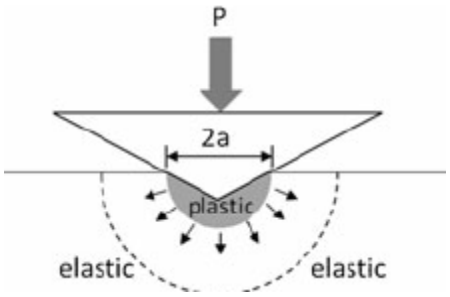

Figure 11 Elastic-plastic Deformation during Indentation Load [38]

The deformation properties can be defined by the relationship between contact pressures p_m with spacemen material yield stress.

Table 7 Deformation Type Depends on Loaded Pressure [37]

$p_m < 1.1Y$	Full elastic response, no permanent or residual impression left in the test specimen after removal of load
$1.1Y < p_m < CY$	Plastic deformation exists beneath the surface but is constrained by the surrounding elastic material, where C is a constant whose value depends on the material and the indenter geometry
$p_m = CY$	Plastic region extends to the surface of the specimen and continues to grow in size such that the indentation contact area increases at a rate the gives little or no increase in the mean contact pressure for further increases in indenter load

The constraint factor in table 7 can be calculated by

$$H \approx CY \tag{2.4}$$

Where hardness (H) commonly use Meyer hardness in indentation test and is given by:

$$H = \frac{P}{A} \tag{2.5}$$

2.2.2 Load-displacement Curve

Load and displacement of the indenter is recorded during Nano-indentation as scattered points and being fitted to a curve automatically by its software.

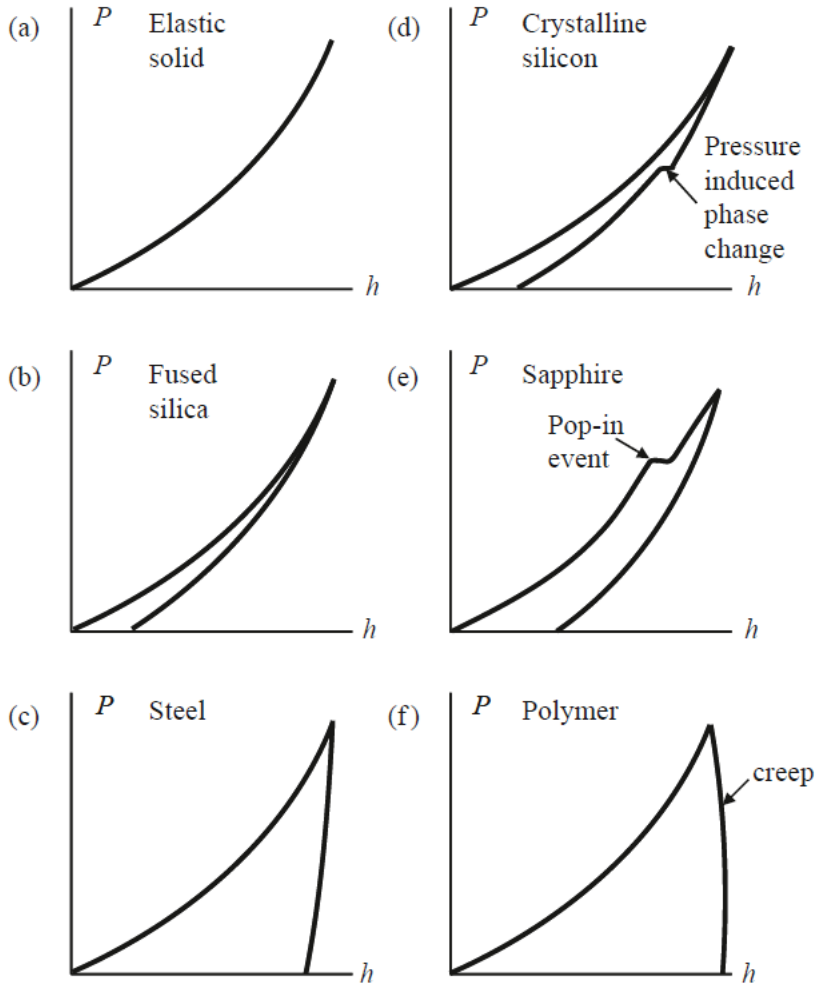

Figure 12 Load-displacement Curves for Different Material.
(a) Elastic solid, (b) brittle solid, (c) ductile solid, (d) crystalline solid, (e) brittle solid with cracking during loading, and (f) polymer exhibiting creep [37]

For pure elastic deformation as shown in figure 12 (a), the force and displacement will arise together and return to zero after the force unloaded. However, plastic deformation is occurred for most material during indentation test, where the indenter feedback force is returned to zero at the position under the initial specimen surface. The difference between initial and ending position reflects the plastic exactly occurred in the spacemen.

2.2.3 Indenter contact area

Contact area is a significant data used in material property calculation which is varied depends on the tip geometry. The general contact area of indenters with same type can be determined by geometry applying on the probes. Fischer-Cripps has been noted the area function given by table 8

Table 8 projected area for different types of indenters [37]

indenter type	projected area	semi-angle
Sphere	$A \approx \pi 2Rh_c$	N/A
Berkovich	$A = 3\sqrt{3}h_c^2\, tan^2\,\theta$	64.27°
Bickers	$A = 4h_c^2\, tan^2\,\theta$	68°
Knoop	$A = 2h_c^2 \tan\theta_1 \tan\theta_2$	$\theta_1 = 86.25°\ \ \theta_2 = 65°$
Cube corner	$A = 3\sqrt{3}h_c^2\, tan^2\,\theta$	34.26°
Cone	$A = \pi h_c^2\, tan^2\,\alpha$	α

However, Nano-indentation is a nanometer scale test, any tiny scratch, damage or deformation of the probes will impact the test result. Indenters are required to calibrate after a long time using. Specific material samples are used in the tip calibrate such as fused silica, which has known

material prosperity and undoubted load-displacement curve. The testing data can be fitted back on the load-displacement curve to calculate the coefficients based on the equation:

$$\mathrm{A} = C_0 h_c^2 + C_1 h_c + C_2 h_c^{1/2} + C_3 h_c^{1/4} + C_3 h_c^{1/8} + C_5 h_c^{1/16} \quad (2.5)$$

Where, C_0 for an ideal Berkovich probe is 23.4.

2.2.4 Hardness and Elastic Modulus calculation for elastic-plastic contact

The elastic modulus and hardness can be determined by the load-displacement curve. A normal load-displacement curve is given in figure 13 (b). h_{max} means the indenter displacement at maximum setting load P_{max}. The length of h_a related the slop $\frac{dP}{dh}$ for the unloading curve at maximum displacement point reflects the equivalents elastic displacement, which is shown the exactly movement of probe from point M to N in Figure 13 (a). The length of h_r is the depth of the residual impression, which shown in Figure 13 (a) is point O to initial point. The h_a means the distance from the contact edge to surface at the full load.

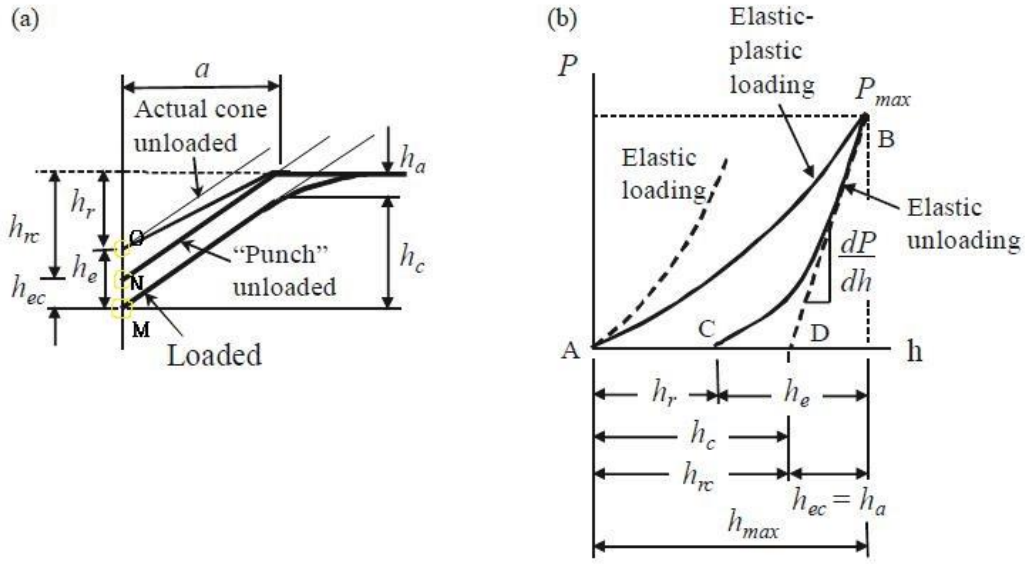

Figure 13 Nano indentation illustration
(a) elastic-plastic contact unload model, (b) load-displacement curve [37]

A common procedure used to determine Hardness and Young's model for Berkovich indenter is to assume that the Berkovich indenter can be equivalence to a conical indenter with a 70.3°face angle, then find the h_{ec} and h_c in Figure 13.

$$h_{ec} = \epsilon \frac{P_{max}}{S} \tag{2.6}$$

Where, ϵ is 0.72 for a conical indenter.

$$h_c = h_{max} - \epsilon \frac{P_{max}}{S} \tag{2.7}$$

Then determined the contact area by calibrate area function

$$\mathrm{A} = C_0 h_c^2 + C_1 h_c + C_2 h_c^{1/2} + C_3 h_c^{1/4} + C_3 h_c^{1/8} + C_5 h_c^{1/16} \tag{2.8}$$

Once the contact area has been determined, the hardness can be calculated by

$$H = \frac{P}{A} \tag{2.9}$$

An advanced model was developed by Oliver-Pharr to using power law fitting constants to determinate the hardness and elastic modulus for those elastic-plastic contact samples. The power low relation was selected to estimate the unloading stiffness [40, 41]

$$P = \alpha(h_{max} - h_r)^m \tag{2.10}$$

Where, α and m are power law fitting constants and can be obtained by fitting the unload curve.

Table 9 Values of Parameters Characterizing Unloading Curves as Observed in Nano-indentation Experiments with a Berkovich Indenter

Material	$\boldsymbol{\alpha\ (mN/nm^m)}$	**m**
Aluminum	0.265	1.38
Soda-line glass	0.0279	1.37
Sapphire	0.0435	1.47
Fused silica	0.0500	1.25
Tungsten	0.141	1.51
Silica	0.0215	1.43

Combined the equations the Young's Module of tested sample can be determined by nano-indentation test with the assumption of Poisson's ratio [44].

$$E = \frac{(1-v^2)}{\frac{2\sqrt{C_0 h_c^2 + C_1 h_c + C_2 h_c^{1/2} + C_3 h_c^{1/4} + C_3 h_c^{1/8} + C_5 h_c^{1/16}}}{a \cdot m (h_{max} - h_r)^{m-1} \cdot \sqrt{\pi}} - \left(\frac{1-v'^2}{E'}\right)} \quad (2.11)$$

Where $E' \; and \; v'$ is the young's module and Poisson's ration for indenter, which are 1141 GPa and 0.07 [43].

Hertz contact model is limited used in elastic model, however, most of hard metal have observably plastic deformation on the surface during nano-indentation. Once a load-displacement curve is obtained for testing sample, Oliver-Pharr method can be applied to determine the equivalent elastic deformation.

2.2.5 Ten percent rule

The ten percent rule is the maximum indentation depth rule to which the maximum setting displace should less than ten percent of the thickness of the testing sample, which is commonly used rule. The mechanical properties measurement in the experiment is obey the ten percent rule

Chapter 3 Experiments procedure and results

3.1 Samples preparation and indenter

3.1.1 Samples observation

Five types samples was received for mechanical property evaluation of magnesium rich primer coated AA 2024 T3 compared with Chromium Primer coating. AA 2024 T3 substrate shown as figure 14 (a), AA 2024 T3 substrate with magnesium rich primer only shown as figure 14 (b), AA 2024 T3 substrate with Chromium Primer only shown as figure 14 (c), top coating over magnesium primer on AA 2024 T3 substrate shown as figure 14 (d) and top coating over Chromium Primer shown as figure 14 (e).

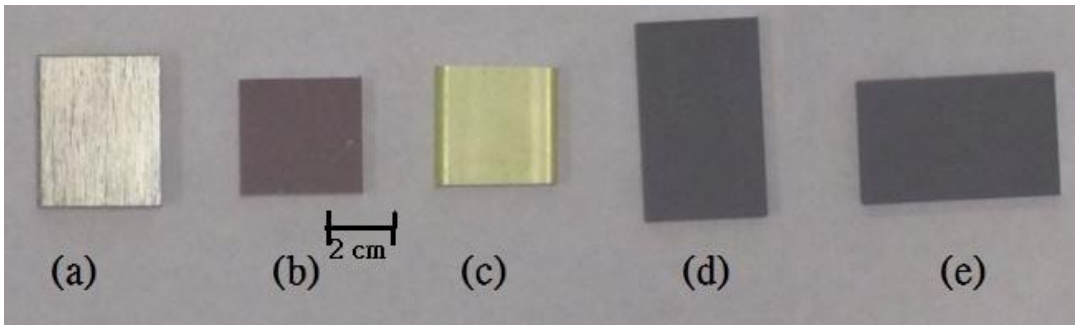

Figure 14 Samples Physical Images

Both high vacuum and low vacuum models of SEM were applied to observe the cross section of the top coated samples with different primer bilayer in order to determine the actual thickness of primer and top coatings.

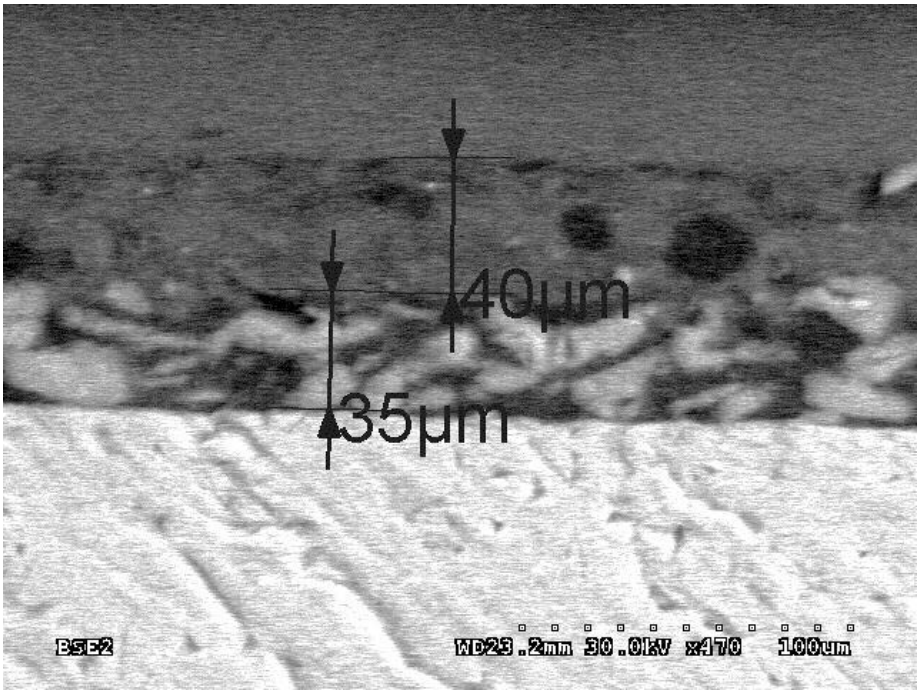

Figure 15 Cross-section of Mg-rich Primer with top coating

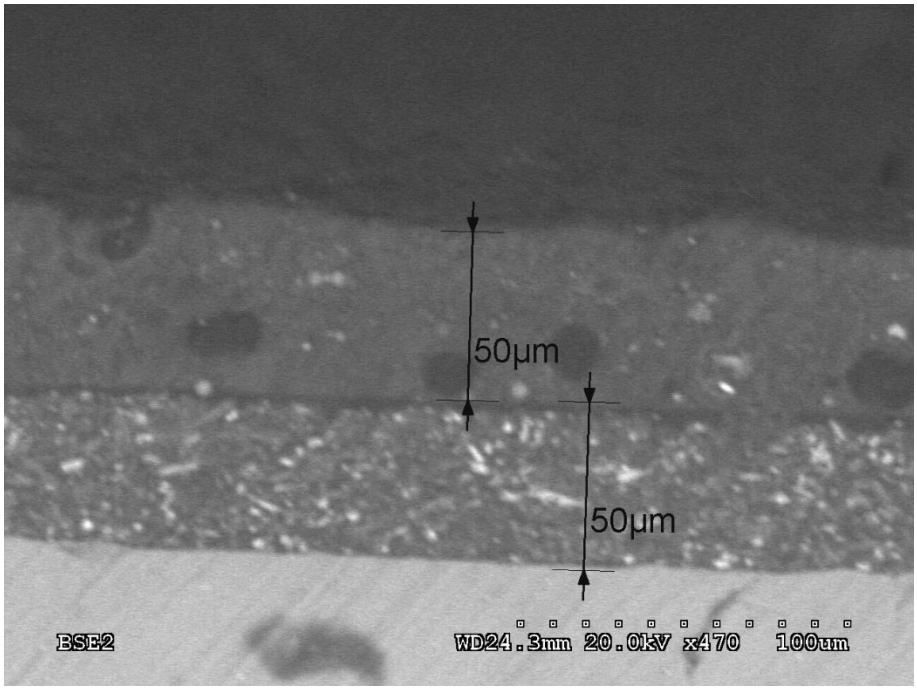

Figure 16 Cross-section of Chromium Primer with top coating

Figure 15 and figure 16 are shown that the cross section of mg-rich primer and its top coating, which are 35 µm and 40 µm, are thicker than Chromium Primer and top coating, which are 50 µm and 50 µm.

Meanwhile, original samples with at least 2cm x 2cm area cannot meet Nano-indentation instrument and SEM sample size requirement, cutting procedure is applied to cut the sample to 1 cm x 1 cm size.

Surface of samples has been observed by SEM. The surface of mg-rich primer has reacted under environment and has been covered by oxidized layer. Since Nano-indentation test is a nanometer scale test, the oxide can significantly impact the Nano-indentation test results. Polishing procedure is chosen to trade the sample surface.

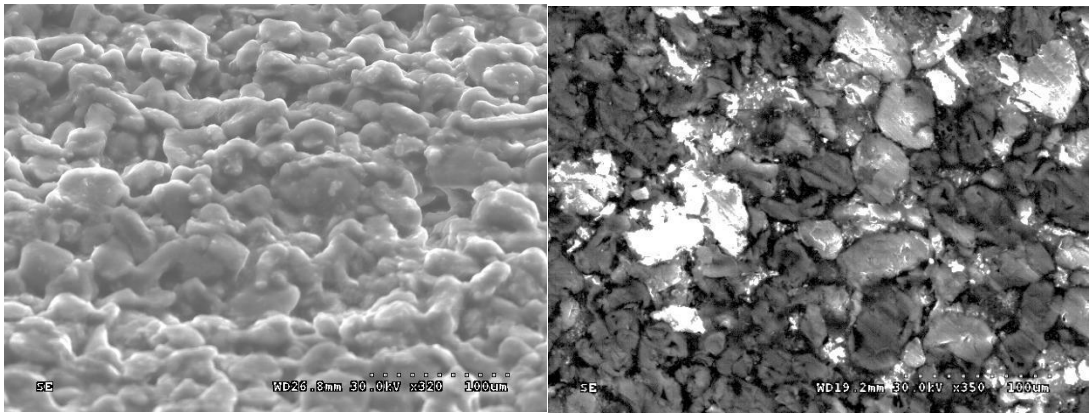

Figure 17 SEM image of Mg-rich primer surface before (left) and after (right) surface polishing

3.1.2 Indenter

Berkovich indenter Ti-0039 which is manufactured by HYSITRON is chosen as test indenter. As shown in figure 18, it has 450 µm of length, 190 µm of radius with 150 µm 150 µm core contact

area (black square area). It is made by diamond (Elastic module 1141 GPa and Poisson's ratio 0.07).

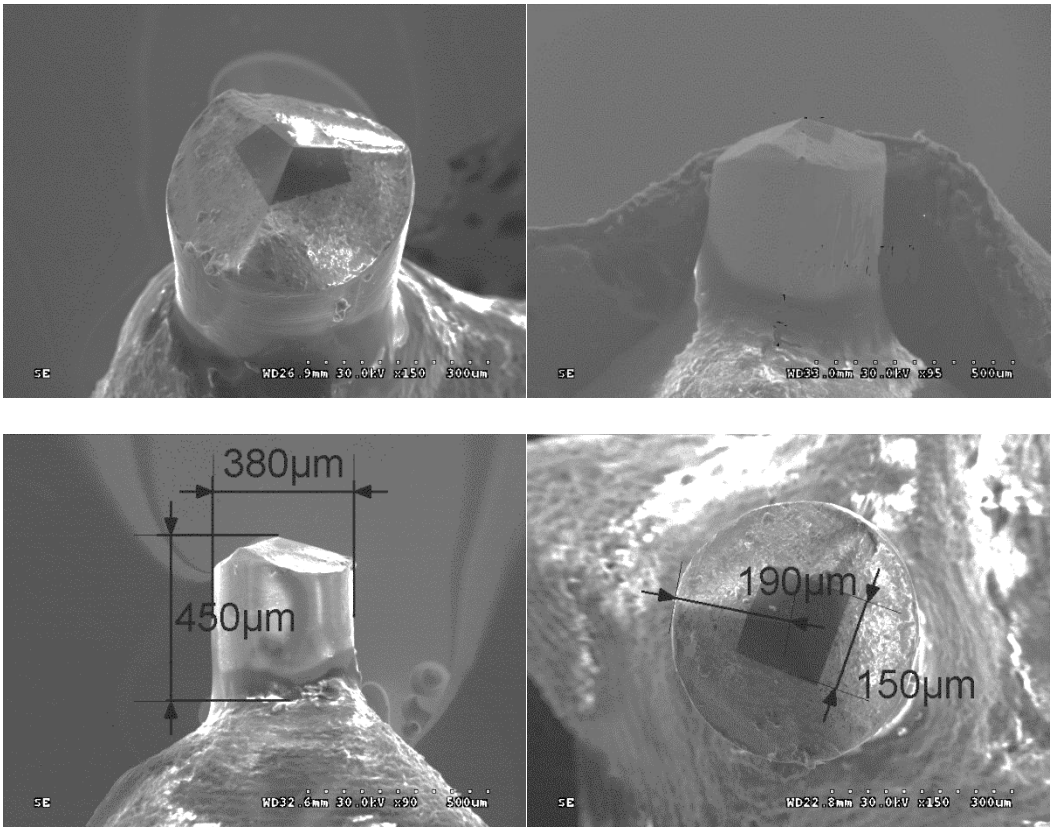

Figure 18 SEM image and size for Selected Berkovich indenter

3.2 Experiments Procedure

3.2.1 Indenter Area Calibration

As talked in Chapter one, Indenter area function calibration is needed before experiments to compensate for non-perfect probe shape, which can correct both of the probe radius of curvature and normal dulling of the probe [44].

The load function used for the probe calibration is an open loop control with 5 second loading time, 2 second holding time and 5 second unloading time as shown in figure 19.

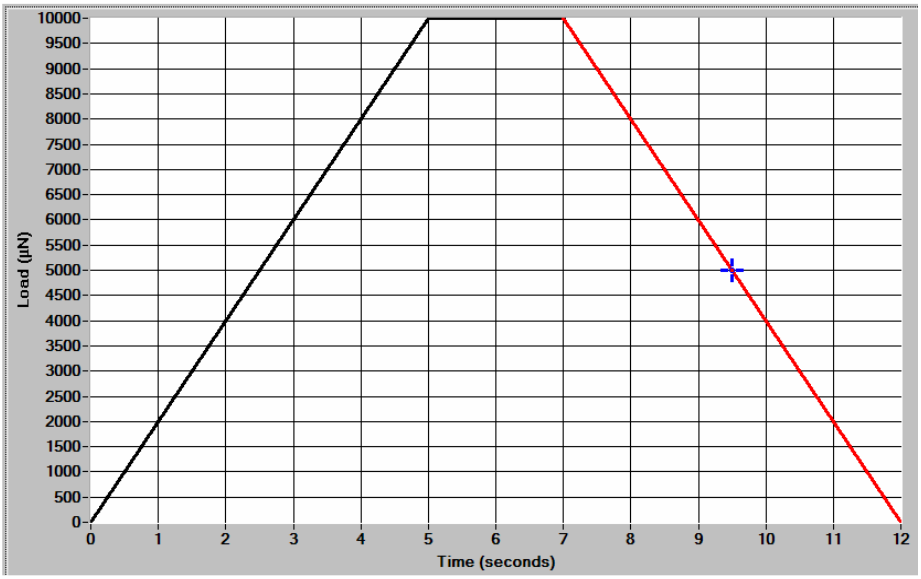

Figure 19 Loading Function of Indenter Area Calibration

The loading function shown in figure 19 is one indent loading cycle is applied on a 5 x 5 array with 5 µm spaces between each indent in a 30 µm of scan size. Loading cycles stars at a high load with 10,000 µN and end with a relatively low load with 100 µN. Thus, 25 load-displacement curves will be recorded for area function analysis.

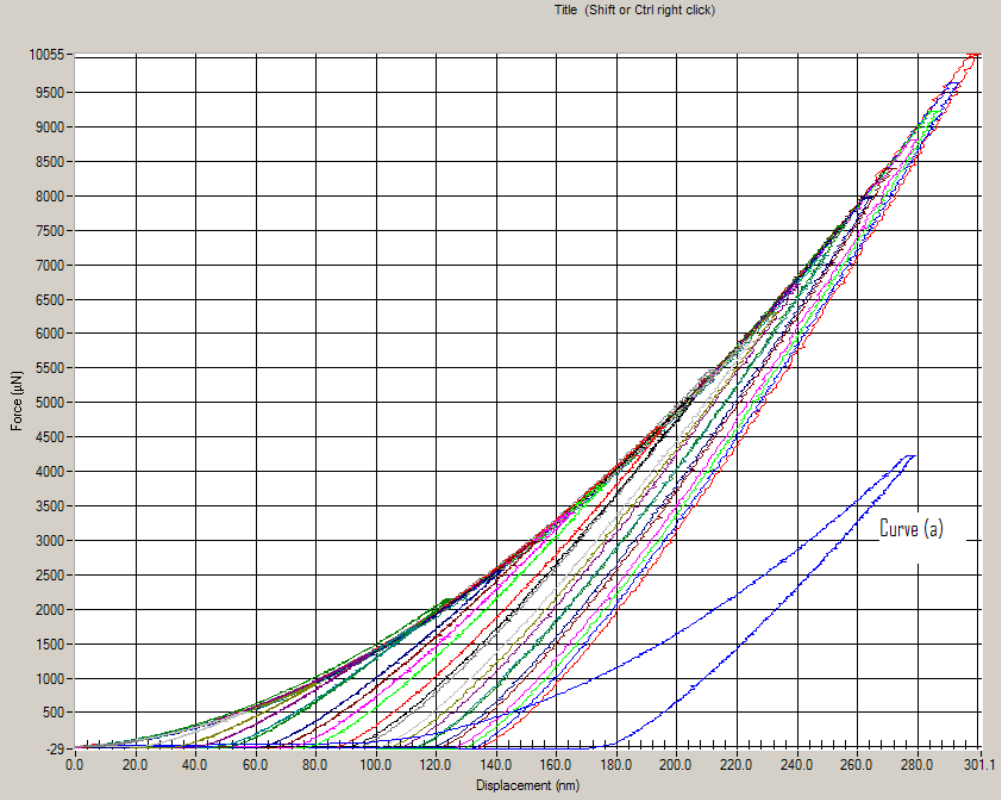

Figure 20 Plot of Probe Calibration Curves

Standard fused quartz sample with known reduced modulus as 69.6 GPa, 9.25 GPa of hardness and 0.17 Poisson's ratio is selected to calibrate tip area. Figure 20 is showing the results of 25 indents, curve (a) is outliers and removed from calculation. An area with contact depth curve shown as figure 20 is generated by load displacement curve.

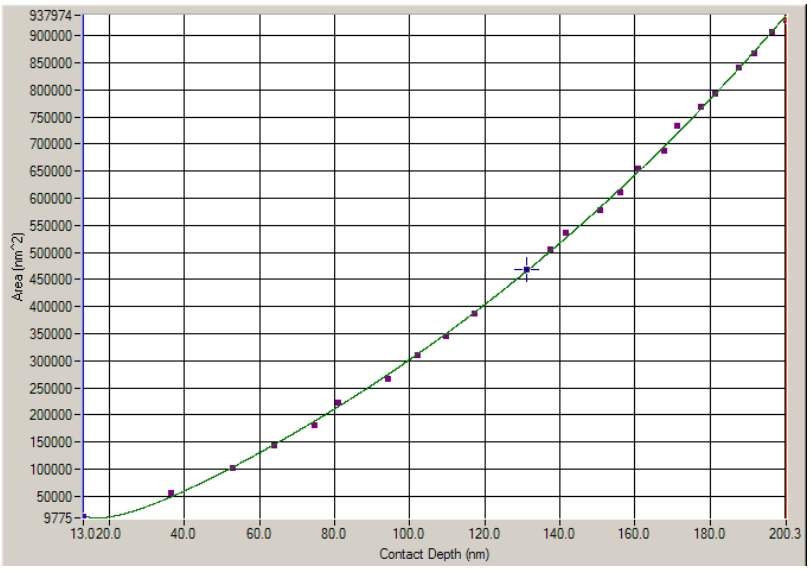

Figure 21 Area with Contact Depth Curve

Equation 2.5 is adopted to fit contact area curve as shown in figure 21 where C_0 is closed to 23.5 for a standard Berkovich probe.

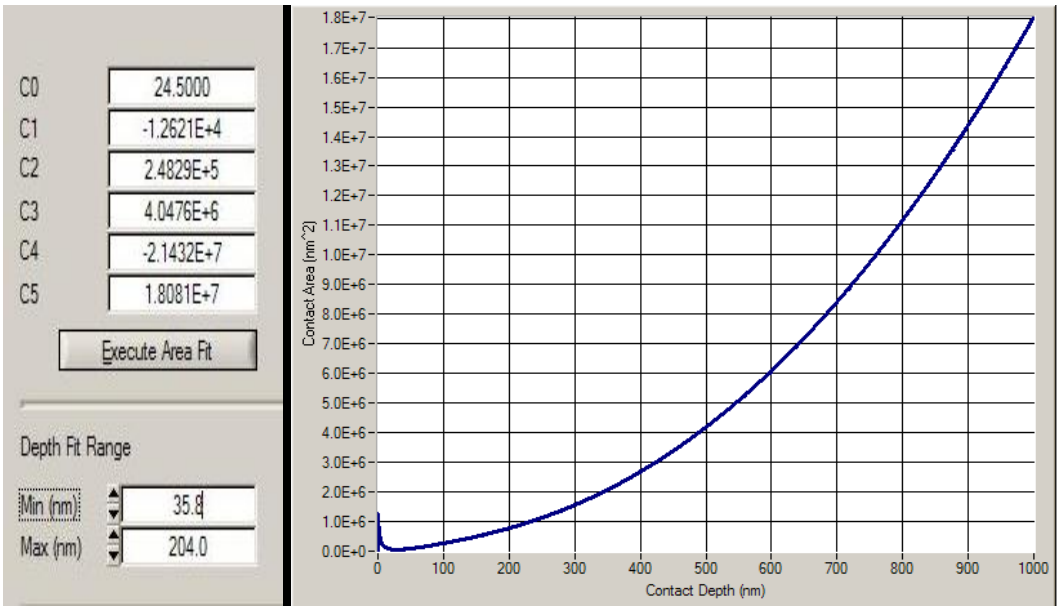

Figure 22 Area Function Coefficient and Plot

Thus, the area function is determined as:

$$A = 23.5h_c^2 - 1.2621 * 10^4 h_c + 2.4829 * 10^5 h_c^{\frac{1}{2}} + 3.0476 * 10^6 h_c^{\frac{1}{4}} - 2.1432 * 10^7 h_c^{\frac{1}{8}} + 1.8081 * 10^7 h_c^{\frac{1}{16}}$$

3.2.2 Load function and indentation cycle

Loading function for all indentation examination in this reasch is 10 seconds loading time, 2 senconds holding time and 10 seconds unloading time as showing in figure 23.

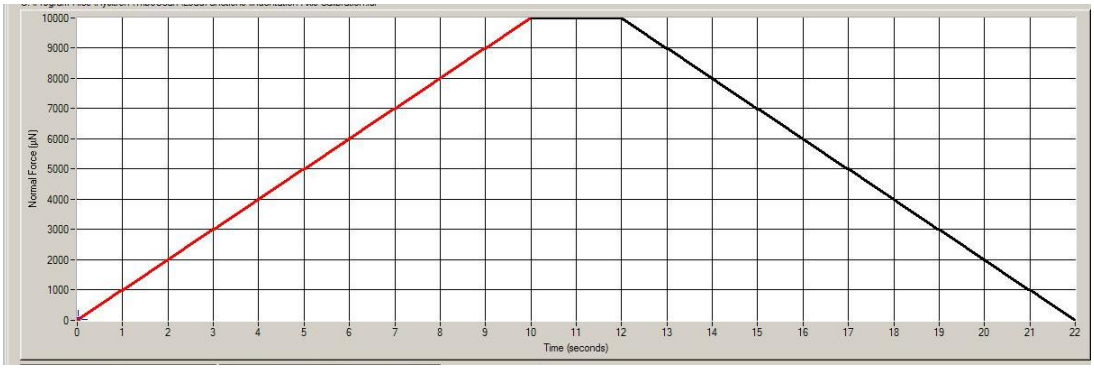

Figure 23 Load Function

However, the maxium load force and loading cycle are various. 500 µN, 1,000 µN, 5,000 µN and 1,0000 µN are applied on different samples, where the displacement caused by miaxium peak load as showing in table 10 can not exceed the ten percent of the coating layer.

Table 10 Maxnium Indentation Displacemenct of Samples

Samples	Displacement by 10,000 μN Loading (nm)	Thickness of testing layer (nm)	Maximum displacement percentage of thickness
Top coating over Chrome primer	1600	50000	3.2%
Top coating over mg-rich primer	1600	40000	3.0%
Chromium Primer coating	1325	50000	2.7%
mg-rich primer coating	1800	35000	4.1%

3.3 Experiment Results

3.3.2 Top Coating over Cr Primer and Top Coating over Mg Rich Primer

For both types of top coated samples, three sets of Nano-indentation test were conducted on top coating layer over the chrome primer. Each set includes 9 indentation points on different 40 μm x 40 μm scaning scetions and the loading function for three sets is shown on figure 24 with different peak load which are 1,000 μN, 5,000 μN and 10,000 μN.

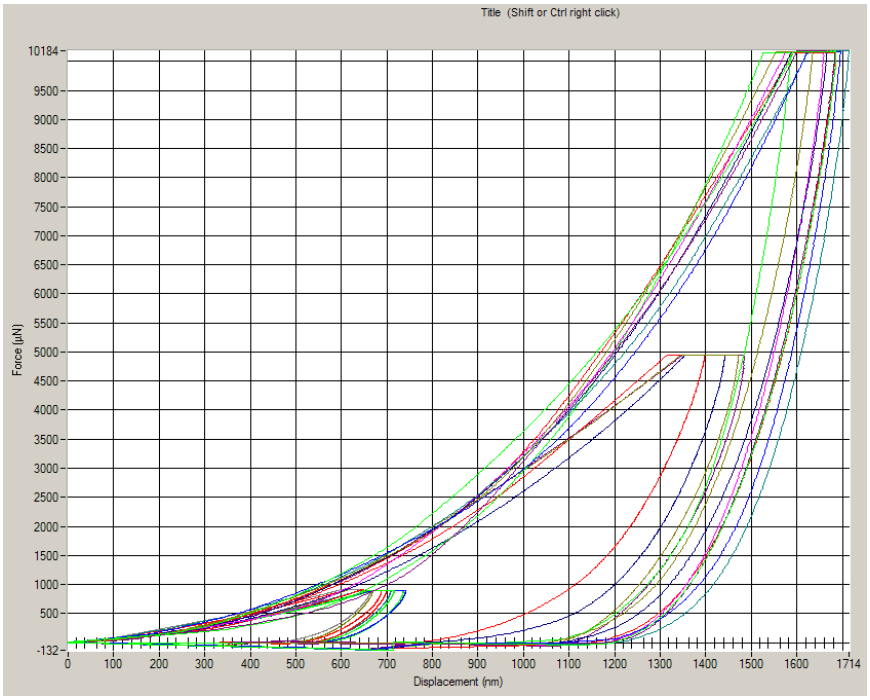

Figure 24 Load displacement curve of indentation on top coating over chromium primer sample

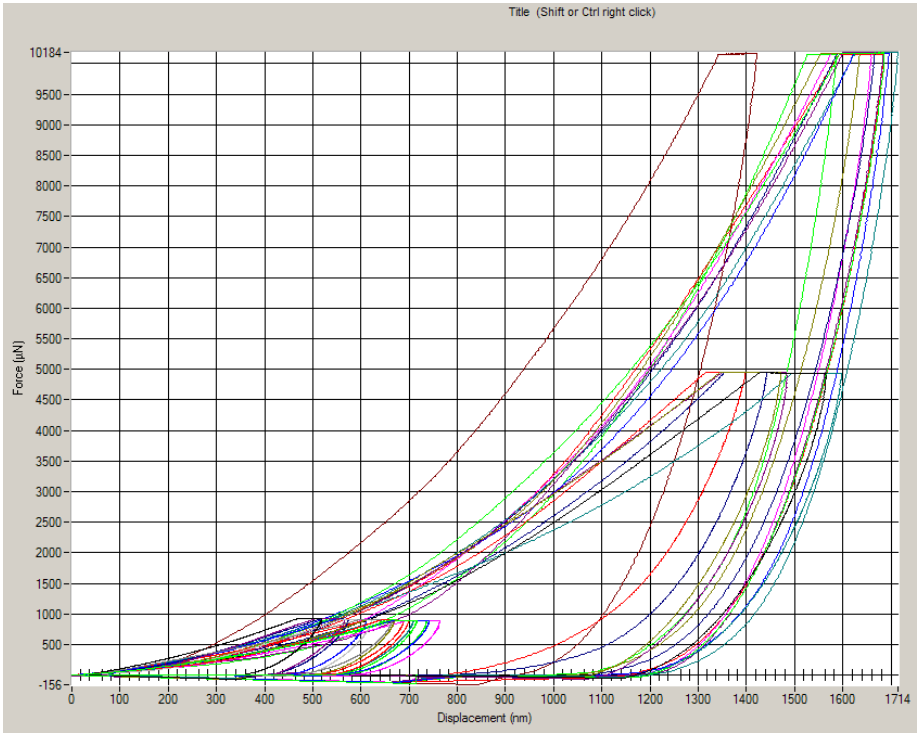

Figure 25 Load displacement curve of indentation on top coating over Mg-rich primer sample

As showing in 3.11 and 3.12, the load displacement curves of 3 sets loading parameters from 500 uN to 10,000 uN only shows elastic-plastic deformation without any delamination occurred. Meanwhile, Similar load displacement behavior shown for Chromium Primer top coating and Mg rich top coating, the unloading part can be used in equation 2.10 to find the power law coefficient, and combined with area function in equation 2.11 to calculate the reduced model, the results are presented in figure 26.

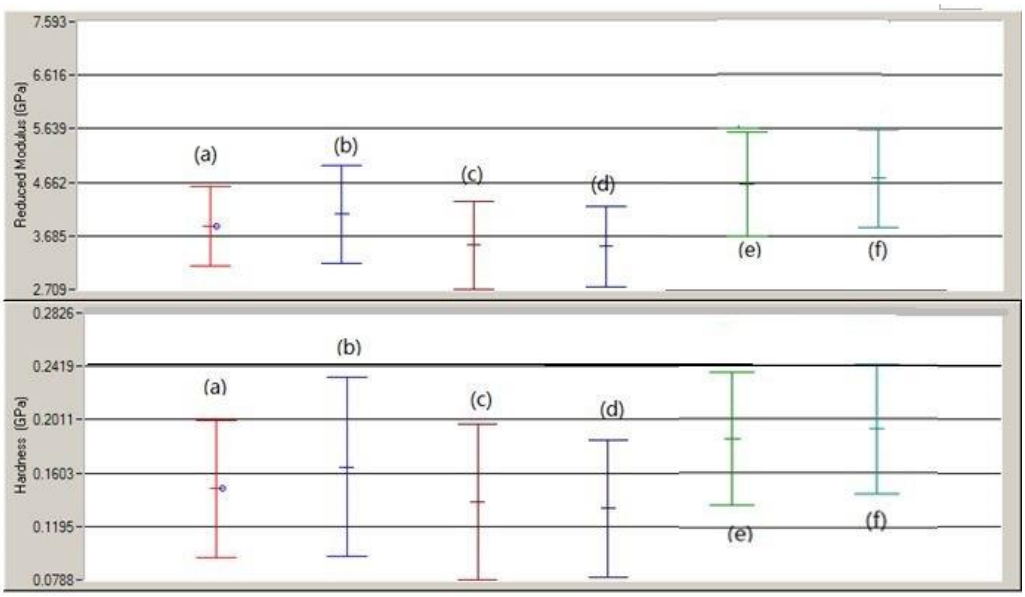

Figure 26 Reduced Modules and Hardness plot of on top coating over Chromium Primer sample and top coating over Mg-rich Primer sample
(a) 1,000 μN peak load on Chromium Primer top coating, (b) 1,000 μN peak load on Mg rich primer top coating, (c) 5,000 μN peak load on Chromium Primer top coating, (d) 5,000 μN peak load on Mg rich primer top coating, (e) 10,000 μN peak load on Chromium Primer top coating, (f) 10,000 μN peak load on Mg rich primer top coating

The reduced modulus in figure 26 is a function of indenter and sample's young's modulus and Poisson's ratio. However, since the diamond indenter has relative high modulus which is 1140 GPa, the reduced modulus can reflects the actual material modulus. Compared with hardness and

reduced modules of top coating on both primer, it can be observed the same property for both sample, it can prove that Mg-rich primer cannot effect the mechanical property on top coating.

3.3.3 Chromium Primer Coating

Three sets of examinations were applied on Chromium Primer coating sample, which is 1,000 μN, 5,000 μN and 10,000 μN. Each set contain 6 indentation points with 10 μm space between every points.

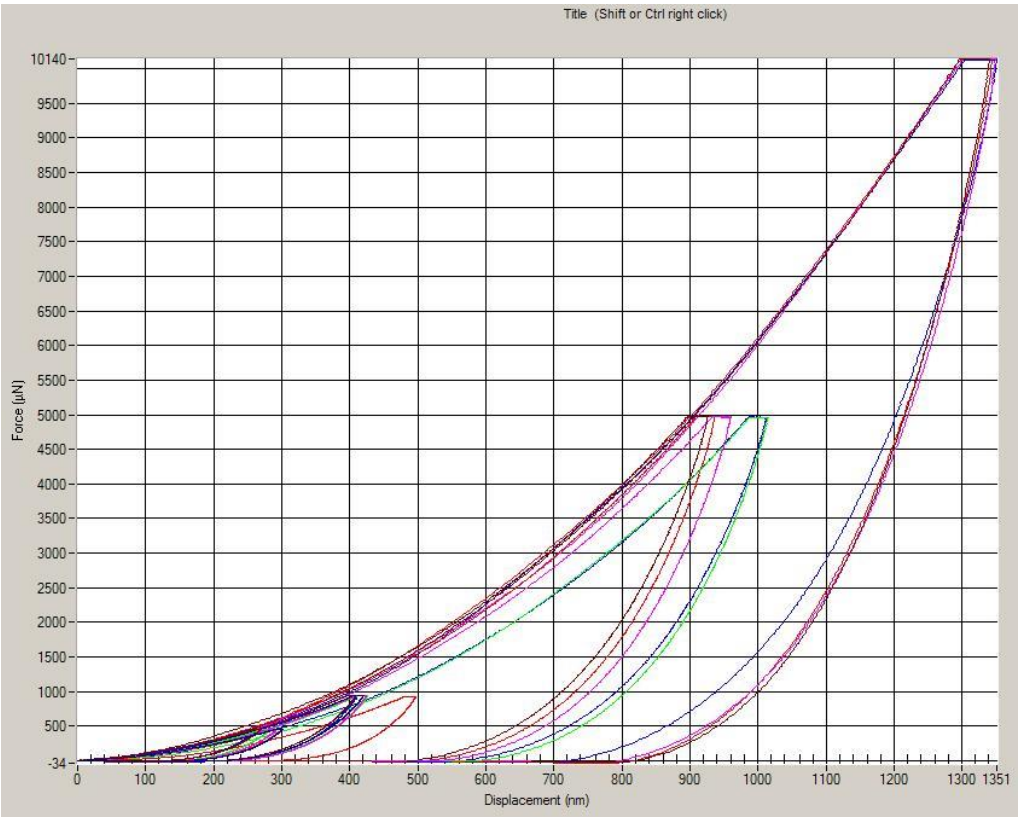

Figure 27 Load displacement curve of indentation on Chromium Primer coating

The unloading part shown in figure 27 can be observed that the 3 sets loading parameters from 500 uN to 10,000 uN only induced elastic-plastic deformation without any delamination occurred. Meanwhile, the curve can be fitted in equation 2.10 to find the power law coefficient,

and combined with area function in equation 2.11 to calculate the reduced model. Results are presented in figure 28.

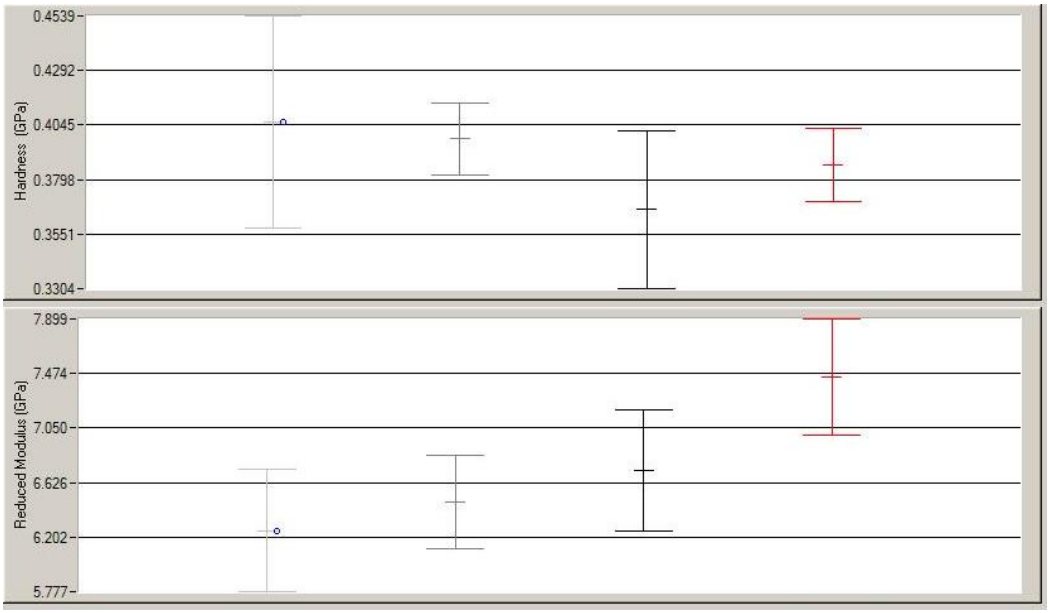

Figure 28 Reduced Modules and Hardness plot of on top coating over Chromium Primer sample and top coating over Mg-rich Primer sample
(a) 1,000 μN peak load, (b) 5,000 μN peak load, (c) 10,000 μN peak load

3.3.4 Magnesium-rich primer coating

Same examinations settings with Chromium Primer coating are applied on mg rich primer coating. However the testing results of load displace curve show various during the same peak load indentation in figure 29,

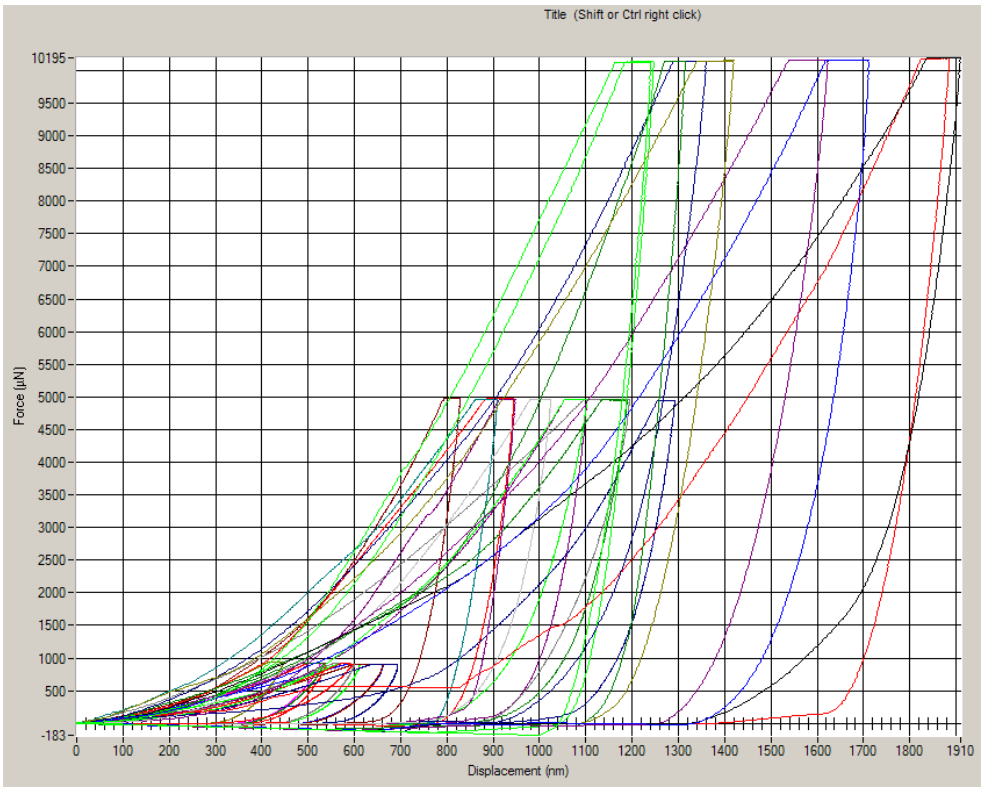

Figure 29 Load displacement curve of Mg-rich Primer coating

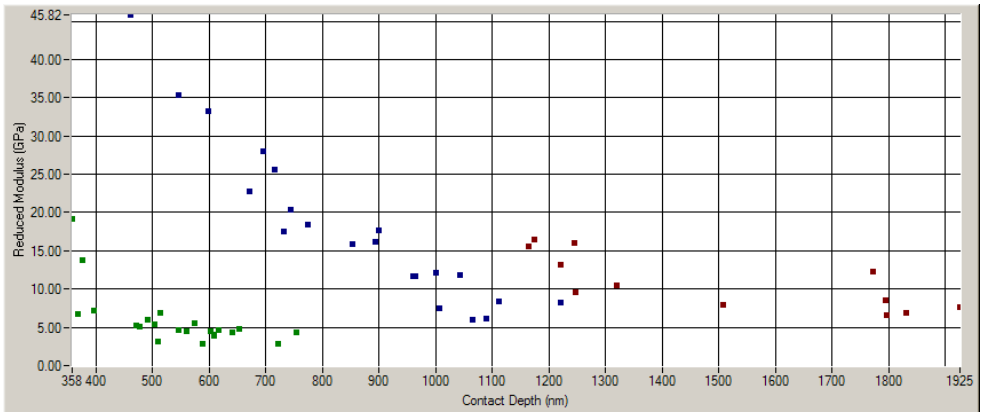

Figure 30 Reduced modulus of Mg-rich primer coating

As showing in figure 29 and figure 30, Mg-primer coating has various loads displace curve and a wide range of reduced modulus from 5 GPa to 35 GPa. However, the load displacement curves for 10,000 µN peak load can be observed to converge to two mean curves. Since contacts regions of Nano-indentation is micro scale, the phenomenon of two mean curves reflects there are two

micro scale components in mg-rich primer. Thus, furfure experiments is applied for mg-rich primer coating to determine its mechanical property

3.3.5 EDS system analysis

SEM image of Mg-rich primer coating surface shows there are different regions in the surface, Mg partial and organic pigment among Mg partials.

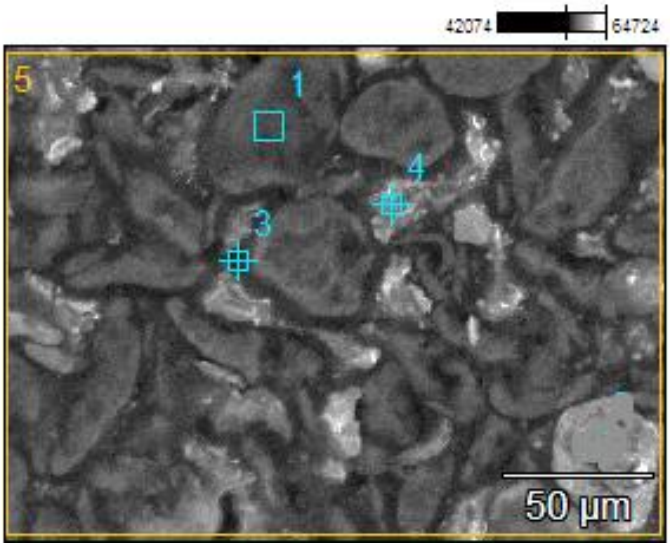

Figure 31 SEM image of Mg-rich surface

Using EDS system of SEM which allowing chemical composition analysis to determine surface compounds on Mg-rich primer coating. From chemical composition analysis result shown in figure 31 can be observed that the compounds of region 1 contain more magnesium element (33.75% weight percentage) that can be defined as Mg piratical in mg-primer coating. However, region 3 around Mg practical contains more Oxygen (12.55% weight percentage) and carbon (74.83% weight percentage) elements can be determined as organic pigments.

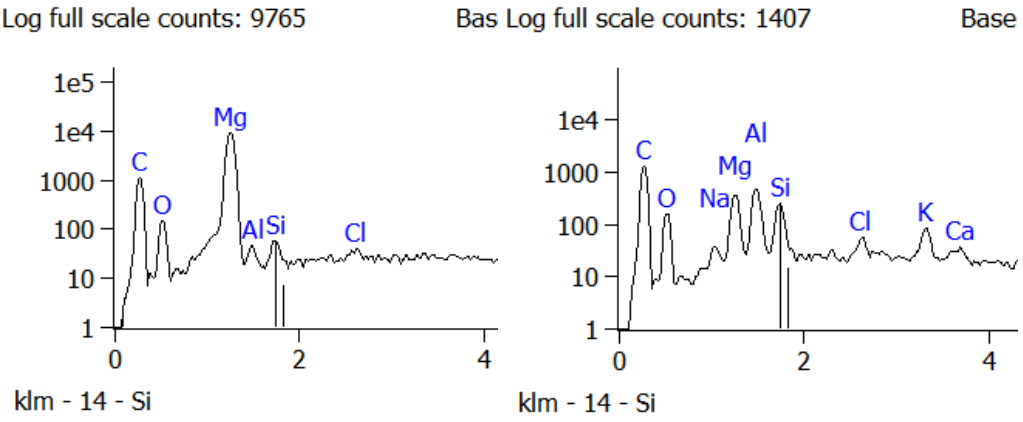

Figure 32 Chemical composition analyses on Mg-rich primer coating surface

Table 11 Weight percentage analyses on Mg-rich primer coating surface

	C-K	*O-K*	*Mg-K*	*Al-K*	*Si-K*	*Cl-K*
Region 1	60.37	3.47	33.75	0.00	0.31	0.10
Region 3	74.83	12.55	3.23	3.08	2.08	0.39
Entire selected surface	57.72	9.17	31.35	0.81	0.48	0.34

Updated nano-indentation experiment setting is used for Mg-rich primer coating which is 16 point indentations at 10,000 μN according to the surface condition to determine the mechanical properties for both of Mg particle and organic pigments. The result is shown in figure 32.

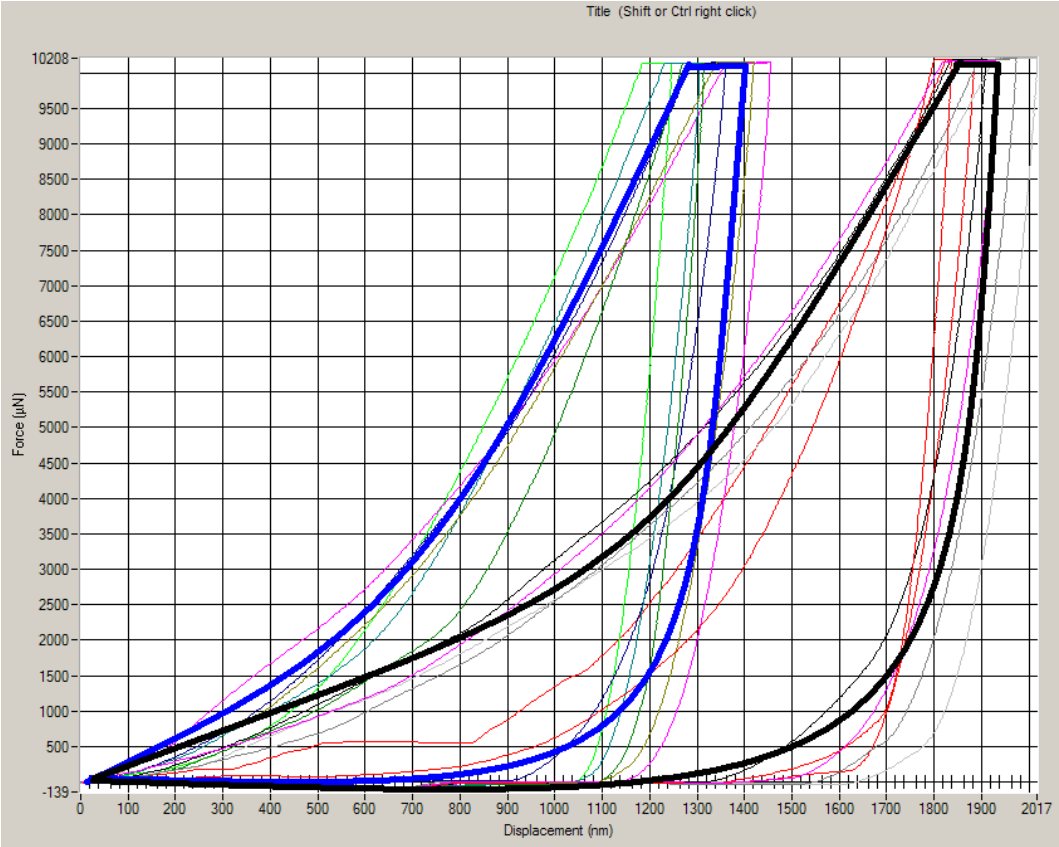

Figure 33 load displacement curve for new indentation test on mg rich primer coating test

Two mean curve can be observed on the load displacement plot. The blue curve reflects the behavior of Mg particle and the black curve reflects the behavior of organic pigments. Only elastic-plastic deformation can be observed under maximum 10,000 uN for both Mg particle and pigment load. Delamination characteristics of load displacement curve cannot be observed under 10,000 uN indentation loading.

3.4 Conclusion

According to the nano-indentation experiment and load displacement data records, only mechanical properties for each coating layer have been determined. Testing results as table 12 shows that average reduced modules for Mg-rich primer coating (10.69 GPa) is higher than

Chromium Primer coating (6.27 GPa). However, the hardness (0.23 GPa) is lower than Chromium Primer coating. Meanwhile, the difference mechanical properties of bilayer coating cannot impact the mechanical properties of top coating surface.

Table 12 Summary of measured mechanical property by nano-indentation

		1,000 μN Peak load	5,000 μN Peak load	10,000 μN Peak load	Average
Top coating on Cr primer	Reduced Modules (GPa)	3.74	3.26	3.86	3.78
	standard deviation	0.61	0.42	0.44	0.51
	Hardness (GPa)	0.14	0.12	0.18	0.14
	standard deviation	0.04	0.02	0.04	0.04
Top coating on Mg rich primer	Reduced Modules(GPa)	3.15	3.27	3.88	3.81
	standard deviation	0.44	0.45	0.42	0.43
	Hardness (GPa)	0.17	0.12	0.19	0.17
	standard deviation	0.02	0.05	0.03	0.04
Cr primer coating	Reduced Modules (GPa)	6.76	6.99	7.51	6.27
	standard deviation	0.37	0.49	0.51	0.58
	Hardness (GPa)	0.43	0.39	0.34	0.35
	standard deviation	0.01	0.03	0.07	0.03
			Mg particle	Organic pigment	Average
Mg-rich primer coating	Reduced Modules (GPa)		13.73	7.33	10.69
	standard deviation		2.42	0.72	3.42
	Hardness (GPa)		0.31	0.14	0.23
	standard deviation		0.01	0.02	0.09

Chapter 4 Finite Element Analysis

Although magnesium primer enhance reliability and protect AA 2024 T3 from corrosion, contrasting micro structure of magnesium primer including relative large magnesium particle distributed in organic pigment compared with Chromium Primer and different material properties can generate various stress distribution to induce film failure between top coating and primer or primer and subtract. Interfacial delamination, which can be generated by increasing indentation load, is commonly observed in indentation experiments. [45, 46] commonly observed in indentation experiments,

FEA method is widely adopted to study the failure of coated system and is employed in this thesis to evaluate the experimental result, and predict the physical phenomenon including elastic-plastic deformation and interface contact deboning with increasing indentation load.

4.1 Governing Equations

4.1.1 Equations of Elastic-plastic deformation

Expanding cavity model is applied to simulate the elastic-plastic behaver in Nano-indentation. For a sharp wedge or conical indenters including the equivalent Berkovich indenter, the module has been demonstrated by numerical simulation for both elastic-perfect plastic and elastic-plastic materials [49]. For the indentation experiments stress-strain curve, equation of elastic-plastic material is employed in FEA:

$$p = \frac{1.273}{(tan23.7)^2}\left(1 + \frac{\sigma_u}{\sigma_y}\right)[1 + \ln(\frac{E*tan23.7}{3\sigma_y})]\sigma_u h_c^2 \quad (4.1)$$

Where p donates mean contact pressure, $\sigma_u$and σ_y represents the ultimate strength and yield strength.

Since the special character of the stress fields of indentation experiment, the simulation is assumed that the specimen materials are isotropic [48]. Thus, the simple model of the isotropic material is adopted following a power law corresponding:

$$\sigma = \begin{cases} E\varepsilon & (\varepsilon < \varepsilon_y) \\ \sigma_y(\frac{\varepsilon}{\varepsilon_y})^n & (\varepsilon \geq \varepsilon_y) \end{cases} \tag{4.2}$$

Where σ denotes the stress, ε the total strain, E the elastic modulus, n the work hardening exponent.

Meanwhile von Mises equivalent stress further is applied as appropriate scalar values to present three-dimensional indentation stress distribution results:

$$\sigma_{VM} = \frac{1}{2}\sqrt{(\sigma_1 - \sigma_2)^2 + (\sigma_2 - \sigma_3)^2 + (\sigma_3 - \sigma_1)^2} \tag{4.3}$$

4.1.2 Formulation of Cohesive Zone Model

The delamination is occurred by contact behavior between indenter and coating, which can be divided as normal and tangential behaviors. Normal contact stress generates deformation of the spacemen. However, tangential stress can induce a penalty-type contact which is an imaginary springs between the master surface and the slave surface [49]. Barenblatt and Dugdale was developed an alternative formulation cohesive zone model (CZM) to formulate interfacial

delamination instead of generally model formulated by fracture approach, CZM is formulated depends on traction separation law, which reflects traction force changing crossed the interface.

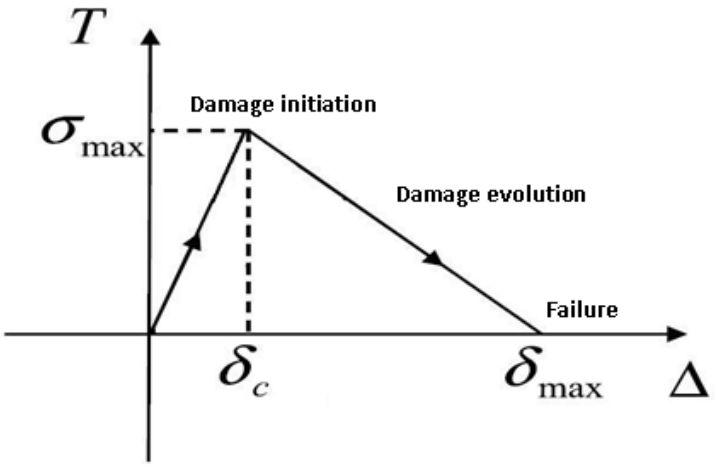

Figure 34 Bilinear Traction-Separation Responses [47]

A typical bilinear traction-separation responses curve is presented in figure 34. Damage initiation is occurred when the cohesive strength and displacement reached at σ_{max} (maximum cohesive strength) and δ_c (characteristic length). Damage evolution which reflect cohesive stiffness than reduce, interface deboning is initiated where the stiffness reduced to zero at failure point ($\delta_{\max}$). The area of the triangle represents the fracture energy [47]. The following equations can describe the bilinear constitutive response [50]:

$$T = \begin{cases} K\delta & (\delta < \delta_c) \\ (I - D)K\delta & (\delta_c \leq \delta < \delta_{\max}) \\ 0 & (\delta \geq 0) \end{cases} \tag{4.4}$$

Where, $T = \begin{bmatrix} T_N \\ T_T \end{bmatrix}$ is the separation stress matrix, $\delta = \begin{bmatrix} \delta_N \\ \delta_T \end{bmatrix}$ is the separation displacement jumps matrix, K = $\begin{bmatrix} K_N & 0 \\ 0 & K_T \end{bmatrix}$ is the undamaged surface stiffness matrix where $K_N = K_T$ since the assumption of isotropic material, D = $\begin{bmatrix} D_N & 0 \\ 0 & D_T \end{bmatrix}$ is the diagonal matrix representing the damage

accumulation at which complete separation is assumed, I is the identity matrix, and subscript $N\ and\ T$ represent the normal and tangent directions.

The critical cohesive energy is determined by:

$$\Gamma^c = \frac{1}{2} T^c \delta_{max} \tag{4.5}$$

Where, $\Gamma^c = \begin{bmatrix} \Gamma_N^c \\ \Gamma_T^c \end{bmatrix}$ is the critical cohesive energy matrix and $T^c = \begin{bmatrix} T_N^c \\ T_T^c \end{bmatrix}$ is the cohesive strength matrix.

Table 13 the Cohesive Zone Parameters [51]

$G_c(J/m^2)$	$\sigma_{max}(Pa)$	$\tau_{max}(Pa)$	ξ
400	25	20	1E-30

As shown in Table 13, the Cohesive Zone parameters for general polymer coating material is assumed in the study.

4.2 Model Geometry

SOLIDWORKS 2015 is employed for creating geometry of Nano-indentation test for FEA. The geometry for a Berkervich indenter is axisymmetric and the size of samples is relative larger than indenter which sharp can be ignore in simulation, only contact area and surrounding area of the sample are defined in mode. Since the problem possesses symmetry with respect to the y-axis, only one sixteen of the geometry is modeled as shown in Figure 35.

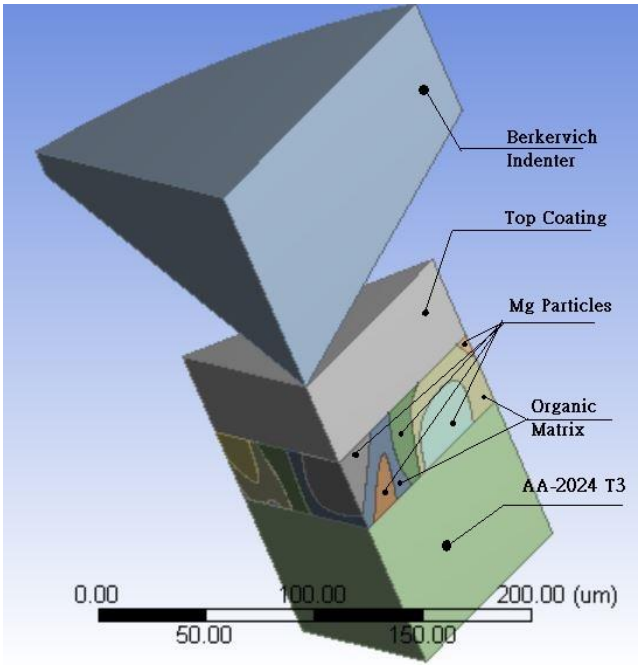

Figure 35 Nano-indentation test geometry of magnesium primer with top coating sample

ANSYS 13 is used for FEA to obtain stress and defamation distributions for both samples with mg-rich primer and samples with Chromium Primer to evaluate mechanical property of mg –rich primer coating.

The cross cutting view is used in this chapter, as shown in figure 36, the cut section crossing that origin solid line is determined as line A view and the cut section crossing the blue line is assigned as line B view.

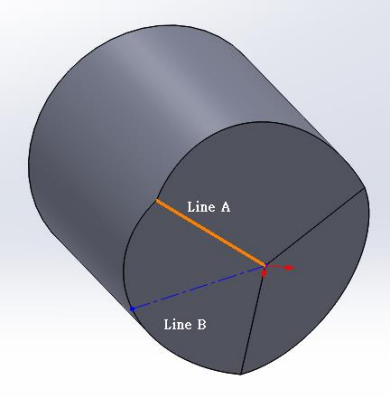

Figure 36 Cross view determine by indenter

Young's modules of top coating obtained in last chapter and assumed passion's ratio are used for material isotropic elasticity in ANSYS. As shown in figure 3.11, maximum load which is 10,184 μN is applied in FEA module. Meanwhile, load function in figure 3.10 is adopted as time peried of FEA module.

4.3 FEA Results

The load displacement behavior tested in Nano-indentation experiment can be proved in FEA, both top coating over Chromium Primer and mg rich primer reflect similar deformation behavior. Thus, top coating over mg rich primer has the same deformation behavior with top coating over Chromium Primer under 10,000 μN Berkovich indentation.

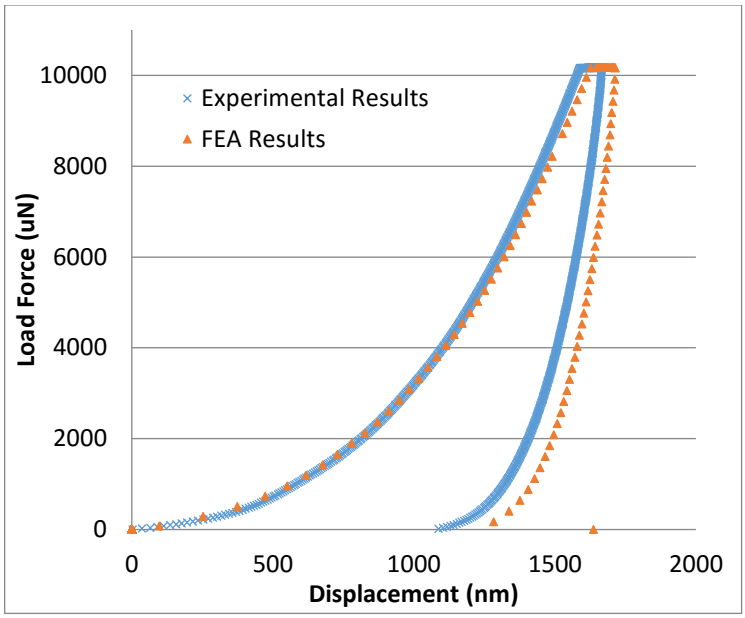

Figure 37 Nano-indentation Experiment Results versus FEA Results on top coating

Figure 37 illustrates load displacement curve of nano-indentation experimental results versus FEA results, which shown that FEA results are generally similar to the experimental result. It is concurred that the elastic-plastic deformation can be simulated by FEA. Thus, the stress distribution simulated by FEA under the indentation loading can be adopted.

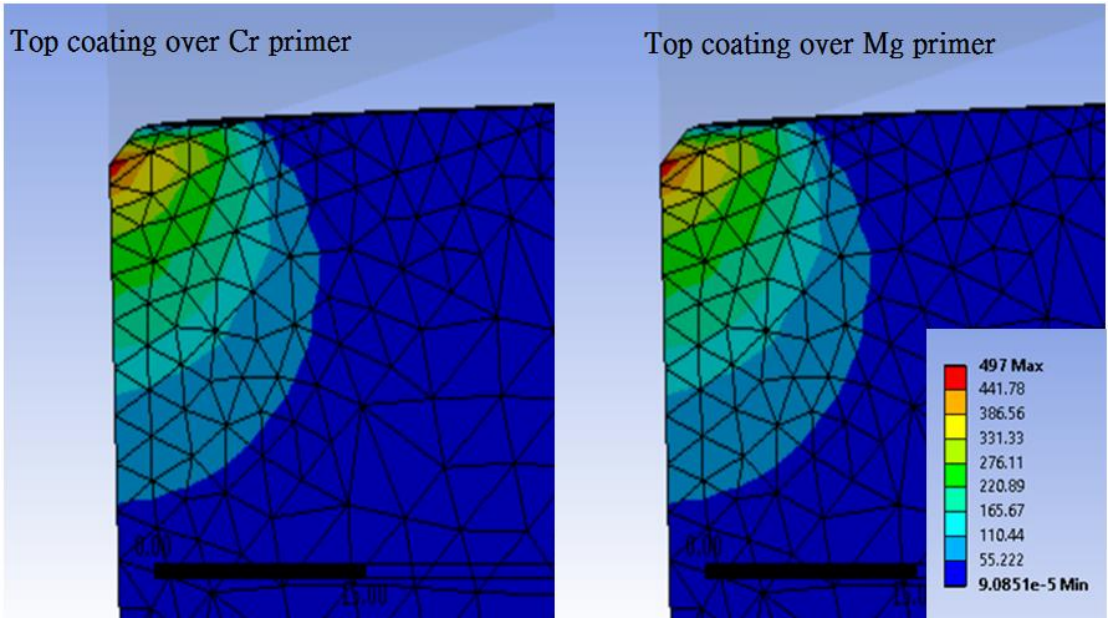

Figure 38 FEA equivalent stress distributions on top coating over mg rich primer and top coating over Cr primer under 10,000 μN loading of Nano-indentation test
(Line A cross section view)

Von Mises equivalent stress is adapted to analysis the stress field under indentation load, which is generated by FEA. The von Mises stress field reveal that the deformation of the top coating thermally grown under the indenter. It is observed that the highest compressive stress occurred in the region right under the indenter tip for top coating surface and the stress only distributed in top coating. The mechanical response in the magnesium rich primer layer is zero when the indentation force is 10,000 uN, which drives 1,800 nm displacement is less than 10% thickness of the top coating (3,500 nm for magnesium top coating and 5,000 nm for chromium top coating). No evidence shows that the underlying primer influence the indentation process of the top coating under 10,000 uN loading.

Since the displacement induced by maximum experiment load is less than 10% thickness of top coating, an increasing load has applied by FEA.

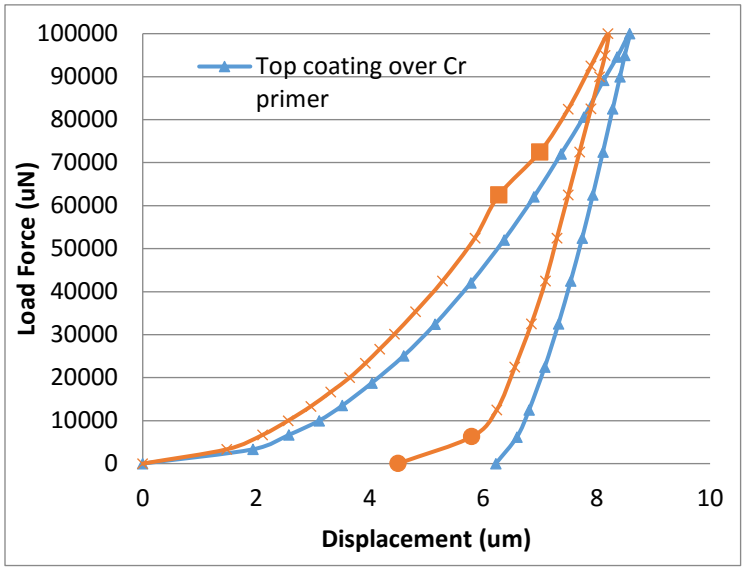

Figure 39 FEA Load displacement curve of top coating over chromium primer verses top coating over magnesium primer

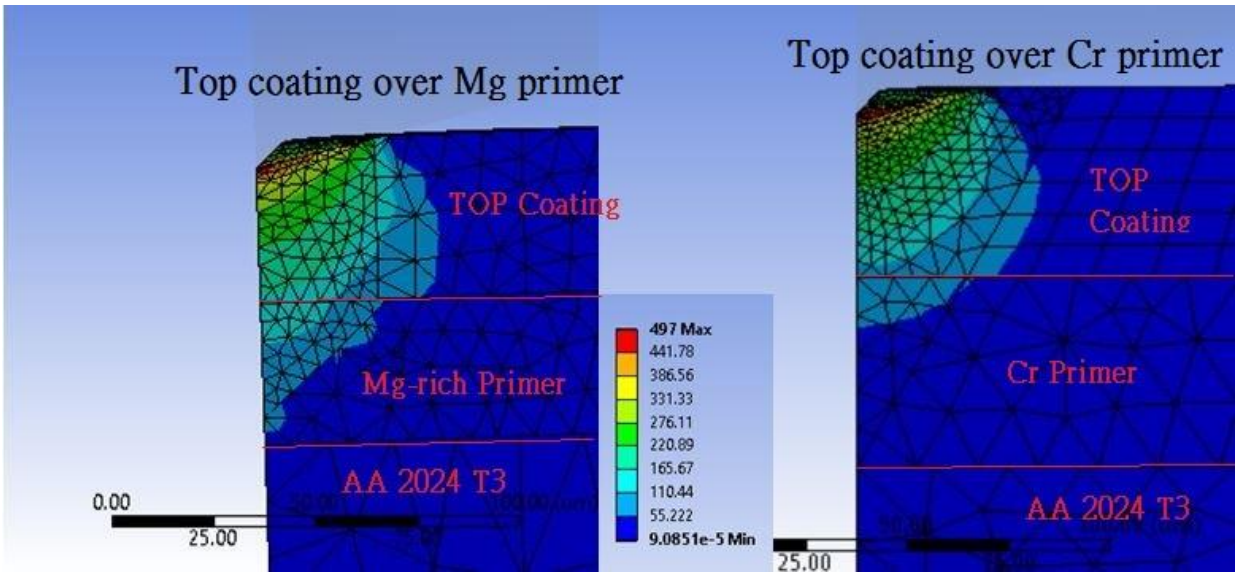

Figure 40 Von Mises Stress fields of top coating over Mg rich primer and Cr primer under 100,000 uN loading

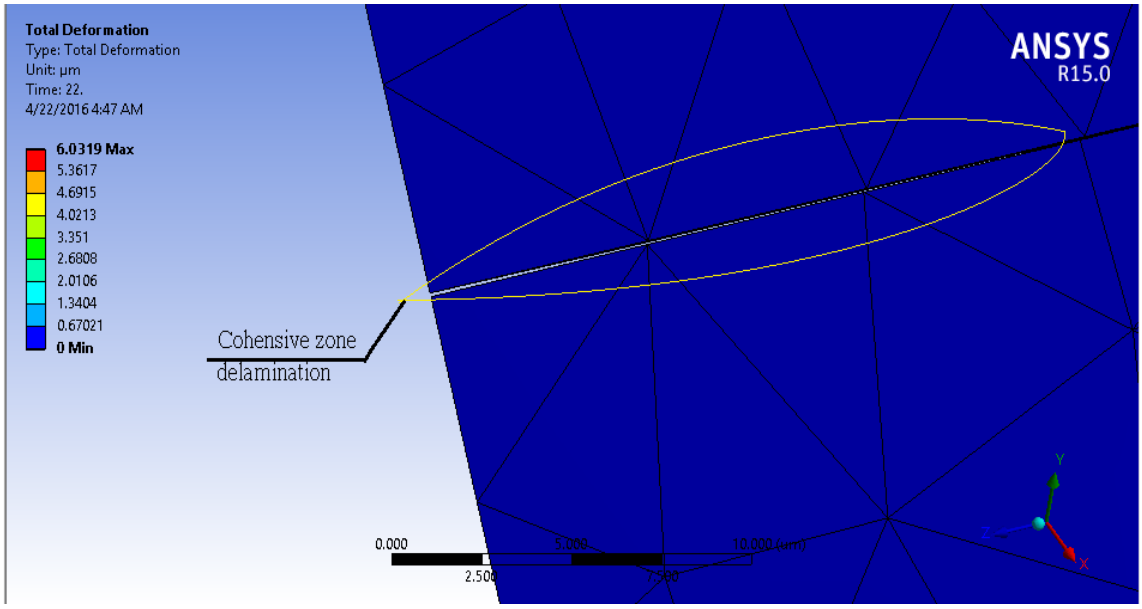

Figure 41 Cohesive zone delamination

The load displacement curve (Figure 39) shown a distinct pop in event occurred at 60,000 uN (between the two square points) and pop out (between the two cycle points) occurred at unloading curve in magnesium rich primer effected top coating, where the delamination was

induced by the tension stress at the interface associated with the mismatch of mechanical properties between top coating and magnesium primer. The delamination of magnesium based top coating is occurred when the indentation load increased to 60,000 μN where the indentation depth is 6.03 μm (20% layer thickness), However, no evidence from load displacement curve shows delamination behavior in chromium primer top coating sample.

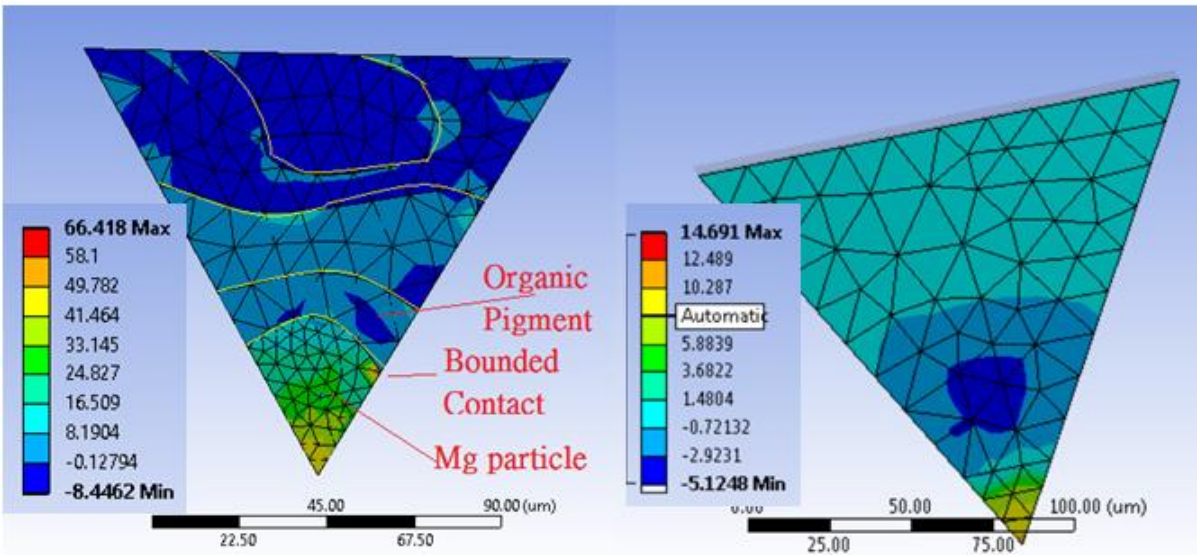

Figure 42 Max Principal stress field on the Mg primer surface (left) and Cr primer surface (right)

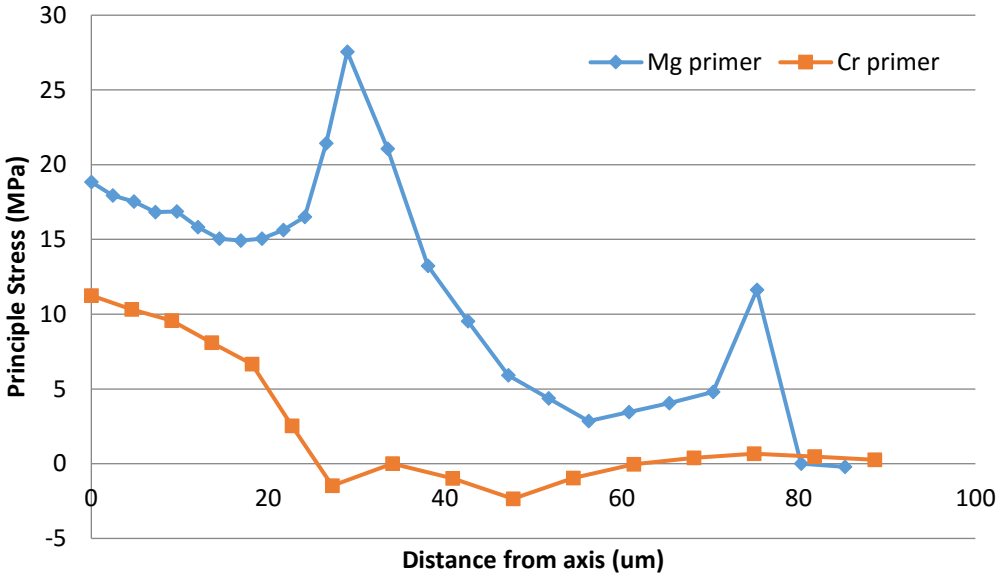

Figure 43 Principal stresses on primer surface along the indentation edge

To better understand the delamination behavior between primer and top coating, the maximum principal stress along the indentation edge, as showing in figure 42 and 43, are illustrated for both magnesium primer and chromium primer. For Cr primer top coating sample, it is demonstrated that the highest tensile stress occurs in the area right beneath the indenter tip and decreased towards along its vertex since the homogeneous micro structure of Cr primer. However, Mg primer has the highest tensile stress concentrated at the boundary between mg particle and organic pigment. Since the different material prosperities of mg primer and top coating, the stress concentrated at the boundary are higher than that in the center area which means that the delamination can be induced starts from the surface edge of mg particle compared with Cr primer top coating sample under the same indentation load.

Chapter 5 Conclusion and Future Work

In this study, experimental and numerical method has been employed to measure and evaluate the magnesium rich primer coating system compare with chromium primer coating system. Nano-indentation experiment was applied to measure the young's module and hardness for each coating material, which has been carried out by FEA. The various load displacement curves of magnesium rich primer recorded from experiment illustrates that the inhomogeneous medium is distributed in the material which has been proved by chemical composition analysis of EDS system. However, different interlayer primer does not affect the top polyurethane coating properties under the maximum 10,000 μN indentation loading in nano-indentation experiment. The loading displacement curves of top coating over Mg rich primer sample and top coating over Cr primer sample have no significant difference which only show regular elastic-plastic deformation under the indentation loading from 1,000 μN to 10,000 μN. There are no evidence shown the interface behavior including delamination or deboning occurred during the experiments.

FEA is applied to evaluate the experiment result. The load displacement curve of simulation is similar with the experimental result. Thus, the accuracy of young's module and hardness measured by experiments can be approved. Meanwhile, The von Mises stress distribution illustrates the similar stress field between top coating samples, which can prove the results from the experiment that interlayer primer cannot affect the top coating material prosperities under maximum 10,000 μN.

Furthermore, in order to predict future behavior along with the increasing indentation loading, cohesive zone model of FEA is introduced to simulate the interface behavior between each layer,

which can characterize the constitutive relation of the interface. Increased indentation loading has been applied in simulation, starts from the limitation loading of the experiment instruction (10,000uN) to 100,000 μN. The load displacement curve for magnesium primer top coating illustrates the delamination characteristic around 60,000 μN loading. Von stress distributions of both samples reflects that the interface stress (around 200 GPa under the center indentation region) affected by stress fluid on magnesium top coating sample is four times as large as the stress in chromium top coating interface under the 100,000 μN. it can also demonstrate that the delamination behavior in the interface between magnesium coating sample is occurred compared with bonded interface between chromium coating under the same indentation loading.

Last but not lease, an investigation of principle stress on the interface along the Berkovich indenter edge has been applied to better understand the delamination behavior. It is shown that the maximum principal stress (27 MPa) is concrete around the boundary of magnesium particle and organic pigment on magnesium coating surface. Delamination is induced by the highest tensile stress concentrated. However, the highest principal stress (12 MPa) of chromium primer top coating occurs in the area right beneath the indenter tip. The phenomena of maximum principal stress represents that the inhomogeneous magnesium rich primer can be easer cause principal stress concentration than homogeneous chromium rich primer, which can cause early interface failure under the same contact stress.

Since the loading limitation of the nano-indentation instrument, only the material properties can be measured. The maximum indentation load (10,000 μN) cannot affect interface behavior on the current samples which has relevant thick top coating. Micro indentation needs to be applied to evaluate FEA results when the loading increased to 100,000 μN. Meanwhile, boundary affect

between magnesium particles and organic pigment does not considerate in this study, they assumed well bonded in this study.

REFERENCE

[1] T. Chudoba, N. Schwarzer, F. Richter, *Steps towards a mechanical modelling of layered systems.* Surface and Coatings Technology, 2002, 154: p. 140-151.

[2] K.J.Martinschitz, R.Daniel, C.Mitterer, J.Keckes, *Stress evolution in CrN/Cr coating system duringthermal straining.* Thin Solid Films, 2008, 516: p. 1972-1976.

[3] E. A. Staley, J. T. Starke, *Application of modern aluminum alloys to aircraft.* Progress in Aerospace Sciences, 1996, 32.2: p. 131-172.

[4] V. K. Agarwala, T. Fort, *Nature of the stable oxide layer formed on an aluminum surface by work function measurements.* Surface Science, 1976, 54.1: p. 60-70.

[5] F. M. Khoshnaw, R. H. Gardi, *Effect of aging time and temperature on exfoliation corrosion of aluminum alloys 2024-T3 and 7075-T6.* Materials and Corrosion, 2007, 58: p. 345-347.

[6] M. R. VanLandingham, T. F. Juliano, M. J. Hagon. *Measuring tip shape for instrumented indentation using atomic force microscopy.* Measurement Science and Technology, 2015, 16: p. 2173-2185.

[7] A. Bolshakov, G. M. Pharr, *Influences of pileup on the measurement of mechanical properties by load and depth sensing indentation techniques.* Journal of Materials Research, 1998: p. 1049-1058.

[8] P. Manach, D. Favier, *Shear and tensile thermomechanical behavior of near equiatomic NiTi alloy*. Materials Science and Engineering, 1997, A222: p. 45-57.

[9] M. R. VanLandingham, T. F. Juliano, M. J. Hagon. *Measuring tip shape for instrumented indentation using atomic force microscopy.* Measurement Science and Technology, 2005, 16: p. 2173-2185.

[10] P. Moine, J.P. Eymery, R.J. Gaboriaud and J. Delafond, *Ion implantation induced amorphous transformation in a Ti-Ni alloy*. Nuclear Instruments and Methods, 1983, B, 209-210 p. 267.

[11] I.B. Obot, N.O. Obi-Egbedi, S.A. Umoren, *Antifungal drugs as corrosion inhibitors for aluminium in 0.1 M HCl.* Corrosion Science, 2009, 51.8, p. 1868-1875.

[12] P.D. Tall, S.Ndiaye, A.C.Beye, Z.Zong, W.O. Soboyejo, H.-J.Lee, A.G.Ramirez, K.Rajan, *Nanoindentation of Ni-Ti thin films,* Material and Manufacturing Processes, 2007, 22: p. 175-179.

[13] T. Chudoba, V. Linss, M. Karniychuk, F. Richter, *Lateral force–displacement measurements - a new technique for the investigation of mechanical surface properties*. Surface & Coatings Technology, 2005, 200: p. 315–320.

[14] P. Moine, J.P. Eymery, R.J. Gaboriaud and J. Delafond, *Ion implantation induced amorphous transformation in a Ti-Ni alloy*. Nuclear Instruments and Methods, 1983, B, 209-210: p. 267.

[15] Staley, J. T., Lege, D. J. *Advances in aluminum alloy products for structural applications in transportation.* Le Journal de Physique, 1993, IV 3.C7: p. 179.

[16] C.K. Chung, P. J. Su, *Material characterization and nanohardness measurement of nanostructured Ta-Si-N film*. Surface & Coatings Technology, 2004, 188-189: 420-424.

[17] R.F. Bunshah, *Handbook of deposition technologies for films and coatings: science, technology, and applications*. 1994, Park Ridge, NJ: Noyes Publications.

[18] F. Caiazzo, V. Alfieri, F. Cardaropoli, et al. *Butt autogenous laser welding of AA 2024 aluminium alloy thin sheets with a Yb: YAG disk laser*. The International Journal of Advanced Manufacturing Technology, 2013, 67.9-12: p. 2157-2169.

[19] I. Zarudi, J. Zou, and L.C. Zhang, *Microstructures of phases in indented silicon: A high resolution characterization*. Applied Physics Letters, 2003, 82-6: p. 874-876.

[20] P. Ocon, A. B. Cristobal, P. Herrasti, et al. *Corrosion performance of conducting polymer coatings applied on mild steel.* Corrosion Science, 2005, 47.3: p. 649-662.

[21] F. Mansfeld, *Electrochemical impedance spectroscopy (EIS) as a new tool for investigating methods of corrosion protection*. Electrochimica Acta. 1990, 35: p. 1531-1543.

[22] H. R. Lawn, E. R. Fuller, *Equilibrium Penny-like Cracks in Indentation Fracture*. Journal of American Ceramic Society, 1975, 10: p. 2016–2024

[23] P. Watts and C. Wiles, *Recent advances in synthetic micro reaction technology.*Chemical Communications, 2007: p. 443-467.

[24] R. G. Buchheit, *Active corrosion protection and corrosion sensing in chromate-free organic coatings.* Progress in Organic Coatings 2003, 47.3: p. 174-182.

[25] M. Kendig, S. Jeanjaquet, R. Addison, et al. *Role of hexavalent chromium in the inhibition of corrosion of aluminum alloys*. Surface and Coatings Technology, 2001, 140.1: 58-66.

[26] J. Zhao, G. Frankel, R. L. McCreery, *Corrosion Protection of Untreated AA-2024-T3 in Chloride Solution by a Chromate Conversion Coating Monitored with Raman Spectroscopy*. Journal of the Electrochemical Society, 1998, 144.7: p. 2258-2263.

[27] A. Sehgal, G. S. Frankel, B. Zoofan, et al. *Pit growth study in Al alloys by the foil penetration technique*." Journal of the Electrochemical Society, 2000, 147.1: p. 140-148.

[28] R.Westergard, M. Bromark, M. Larsson, P. Hedenqvist, S. Hogmark, *Mechanical and tribological characterization of DC magnetron sputtered tantalum nitride thin films*. Surface & Coatings Technology, 1997, 97: p. 779–784.

[29] A. M. Simoes, D. Battocchi, D. E. Tallman, et al. *SVET and SECM imaging of cathodic protection of aluminium by a Mg-rich coating.* Corrosion Science, 2007, 49.10: p. 3838-3849.

[30] H. P. Godard, W. B. Jepson, M. R. Bothwell, et al. *The Corrosion of Light Metals*. John Wiley & Sons Inc, 1967.

[31] S. Pietsch, W. D. Kaiser, M. Stratmann, *Corrosion-protective effect of organic coatings at the defect–influence of surface preparation and anti-corrosive pigments of base coating.* Materials and Corrosion-Werkstoffe und Korrosion, 2002, 53: 299-304.

[32] D. Bernoulli, U. Müller, M. Schwarzenberger, R. Hauert, R. Spolenak, *Magnetron sputter deposited tantalum and tantalum nitride thin films: An analysis of phase, hardness and composition.* Thin Solid Films, 2013, 548: p. 57–161.

[33] S. Nakao, M. Numata, T. Ohmi, *Thin and low-resistivity tantalum nitride diffusion barrier and giant-grain copper interconnects for advanced ULSI metallization.* Japanese Journal of Applied Physics, 1999, 38: p. 2401–2405.

[34] H. Hertz, *On the contact of solid elastic bodies*. Journal für die reine und angewandte Mathematik, 1881, 92: p. 156–171.

[35] N. Zaafarani, *Three-dimensional investigation of the texture and microstructure below a nanoindent in a Cu single crystal using 3D EBSD and crystal plasticity finite element simulations.* Acta Materialia, 2006, 54.7: p. 1863-1876.

[36] N. N. Huynh, *A study of microstructural evolution around crack tip using crystal plasticity finite-element method.* Proceedings of the Institution of Mechanical Engineers Part J-Journal of Engineering Tribology, 2008, 222.J3: p. 183-192.

[37] P. Peralta, *Characterization of surface deformation around vickers indents in monocrystalline materials.* Metallurgical and Materials Transactions a-Physical Metallurgy and Materials Science, 2004. 35.A.8: p. 2247-2255.

[38] A.C. Fischer-Cripps, “Elastic–plastic response of materials loaded with a pherical indenter,”J. Mater. Sci. 32 3, 1997, pp. 727–736.

[39] W. C. Oliver and G. M. Pharr, *Measurement of hardness and elastic modulus by instrumented indentation: Advances in understanding and refinements to methodology.* Journal of Materials Chemistry, 2003, 19.1: p. 3–20.

[40] W.C. Oliver, G.M. Pharr, *An improved technique for determining hardness and elastic modulus using load and displacement sensing indentation experiments*, Journal of Materials Chemistry, 1992, 7.8: p. 1564-1583

[41] T. Oku, E. Kawakami, M. Uekubo, M. Murakami, K. Takahiro, S. Yamaguchi, *Diffusion barrier property of TaN between Si and Cu.* Applied Surface Science, 1996, 99.4: p. 265–272.

[42] N.A. Sakharova, *Comparison between Berkovich, Vickers and conical indentation tests: A three-dimensional numerical simulation study*. International Journal of Solids and Structures, 2009, 46.5: p. 1095-1104.

[43] C. Gautier, H. Moussaoui, F. Elstner, J. Machet, *Comparative study of mechanical and structural properties of CrN films deposited by d.c. magnetron sputtering and vacuum arc evaporation.* Surface and Coatings Technology, 1996, 86-87: p. 254–262.

[44] M. Pourbaix, *Applications of electrochemistry in corrosion science and in practice*. Corrosion Science, 1973, 14: p. 25-82.

[45] Z. Shi, *The equivalent axisymmetric model for Berkovich indenters in power-law hardening materials.* International Journal of Plasticity, 2010, 26.1: p. 141-148.

[46] S.K. Kim, B.C. Cha, *Deposition of tantalum nitride thin films by D.C. magnetron sputtering.* Thin Solid Films, 2005, 475: p. 202–207.

[47] Y. Liu, *Combined numerical simulation and nanoindentation for determining mechanical properties of single crystal copper at mesoscale*. Journal of the Mechanics and Physics of Solids, 2005, 53.12: p. 2718-2741.

[48] J.J. Vlassak, W.D. Nix, *Measuring the elastic properties of anisotropic materials by means of indentation experiments.* Journal of the Mechanics and Physics of Solids, 1999, 42.8: 1223-1244.

[49] P. Colombi, A. Bassetti, and A. Nussbaumer, *Delamination effects on cracked steel members reinforced by prestressed composite patch.* Theoretical and Applied Fracture Mechanics, 2003, 39(1): p. 61-71.

[50] S. Veprek, *Degradation of superhard nanocomposites by built-in impurities.* Journal of Vacuum Science & Technology B, 2004, 22.2: p. L5-L9.